The Astrophysical Journal, 970:86 (17pp), 2024 July 20 https://doi.org/10.3847/1538-4357/ad4ce3

AGEL: Is the Conflict Real? Investigating Galaxy Evolution Models Using Strong Lensing at $0.3 < z < 0.9$

Nandini Sahu[1,2], Kim-Vy Tran[2,3,4], Sherry H. Suyu[5,6,7], Anowar J. Shajib[8,9,17], Sebastian Ertl[5,6], Glenn G. Kacprzak[2,10], Karl Glazebrook[2,10], Tucker Jones[11], Keerthi Vasan G. C.[11], Tania M. Barone[2,4,10], A. Makai Baker[12], Hannah Skobe[8], Caro Derkenne[2,13], Geraint F. Lewis[14], Sarah M. Sweet[2,15], and Sebastian Lopez[16]
[1] University of New South Wales, Sydney, NSW 2052, Australia; n.sahu@unsw.edu.au
[2] The ARC Centre of Excellence for All Sky Astrophysics in 3 Dimensions (ASTRO 3D), Australia
[3] Center for Astrophysics, Harvard & Smithsonian, Cambridge, MA 02138, USA
[4] University of New South Wales, Sydney, NSW, Australia
[5] Technical University of Munich, TUM School of Natural Sciences, Department of Physics, James-Franck-Straße 1, 85748 Garching, Germany
[6] Max-Planck-Institut für Astrophysik, Karl-Schwarzschild Straße 1, 85748 Garching, Germany
[7] Academia Sinica Institute of Astronomy and Astrophysics (ASIAA), 11F of ASMAB, No.1, Section 4, Roosevelt Road, Taipei 10617, Taiwan
[8] Department of Astronomy & Astrophysics, The University of Chicago, Chicago, IL 60637, USA
[9] Kavli Institute for Cosmological Physics, University of Chicago, Chicago, IL 60637, USA
[10] Centre for Astrophysics and Supercomputing, Swinburne University of Technology, Hawthorn, Victoria 3122, Australia
[11] Department of Physics and Astronomy, University of California, Davis, 1 Shields Avenue, Davis, CA 95616, USA
[12] School of Physics and Astronomy, Monash University, Clayton, VIC 3800, Australia
[13] Astrophysics and Space Technologies Research Centre, School of Mathematical and Physical Sciences, Macquarie University, NSW 2109, Australia
[14] Sydney Institute for Astronomy, School of Physics A28, The University of Sydney, NSW 2006, Australia
[15] School of Mathematics and Physics, University of Queensland, Brisbane, QLD 4072, Australia
[16] Departamento de Astronomía, Universidad de Chile, Camino el Observatorio 1515, Las Condes, Santiago, Chile

Received 2024 February 2; revised 2024 April 30; accepted 2024 May 15; published 2024 July 18

Abstract

Observed evolution of the total mass distribution with redshift is crucial to testing galaxy evolution theories. To measure the total mass distribution, strong gravitational lenses complement the resolved dynamical observations that are currently limited to $z \lesssim 0.5$. Here we present the lens models for a pilot sample of seven galaxy-scale lenses from the `ASTRO3D` Galaxy Evolution with Lenses (`AGEL`) survey. The `AGEL` lenses, modeled using HST/WFC3-F140W images with Gravitational Lens Efficient Explorer (GLEE) software, have deflector redshifts in the range $0.3 < z_{\rm defl} < 0.9$. Assuming a power-law density profile with slope γ, we measure the total density profile for the deflector galaxies via lens modeling. We also measure the stellar velocity dispersions ($\sigma_{\rm obs}$) for four lenses and obtain $\sigma_{\rm obs}$ from `SDSS-BOSS` for the remaining lenses to test our lens models by comparing observed and model-predicted velocity dispersions. For the seven `AGEL` lenses, we measure an average density profile slope of -1.95 ± 0.09 and a γ–z relation that does not evolve with redshift at $z < 1$. Although our result is consistent with some observations and simulations, it differs from other studies at $z < 1$ that suggest the γ–z relation evolves with redshift. The apparent conflicts among observations and simulations may be due to a combination of (1) systematics in the lensing and dynamical modeling; (2) challenges in comparing observations with simulations; and (3) assuming a simple power law for the total mass distribution. By providing more lenses at $z_{\rm defl} > 0.5$, the `AGEL` survey will provide stronger constraints on whether the mass profiles evolve with redshift as predicted by current theoretical models.

Unified Astronomy Thesaurus concepts: Strong gravitational lensing (1643); Galaxy evolution (594); Galaxy mergers (608); Dark matter (353); Early-type galaxies (429)

1. Introduction

In standard cosmology, galaxies form via baryonic and dark matter assembly in the overdense centers of cold dark matter halos (Blumenthal et al. 1984; White & Frenk 1991). Further, galaxies grow their mass and morphology via mergers and environmental processes (Somerville & Davé 2015). To test galaxy evolution theories and various elements adopted in simulations, such as the cosmological model, the properties of dark matter and its dynamics with baryons, baryonic feedback, and subgrid physics, comparisons of observed evolution of total mass distribution with cosmological simulations are essential.

To measure the total baryonic plus dark matter halo mass distribution, gravitational lensing is a powerful tool from galactic (kiloparsec) to cluster (megaparsec) scales (e.g., see Blandford & Narayan 1992; Treu 2010; Shajib et al. 2022b). Gravitational lensing only depends on the total mass distribution of the deflector (also called the lens), and it is independent of the deflector's luminosity or composition. Galaxy-scale strong lenses, where the deflector is a single galaxy, can be used to measure the total mass distribution of the deflector galaxy at high redshifts (e.g., Sonnenfeld et al. 2013a), which is otherwise measured using resolved kinematic observations that are currently limited to lower redshifts ($z \lesssim 0.5$, Derkenne et al. 2023).

The mass distribution of deflectors in galaxy-scale lenses is commonly represented by a radial power-law density profile,

---

[17] NHFP Einstein Fellow.

$\rho \propto r^{\gamma}$, with a constant effective slope $\gamma < 0$ (Treu & Koopmans 2002). The observed evolution of density profile slope with redshift, i.e., the γ–z relation, is compared with the predictions from simulations to examine the galaxy evolution theories. This investigation has been limited to early-type galaxies (ETGs) because, in the current observational settings, the deflectors in the observed galaxy-scale lens samples are commonly massive ETGs (e.g., Bolton et al. 2006).

Galaxies are theorized to evolve broadly in two phases (Naab et al. 2007; Guo & White 2008; Oser et al. 2010). In the first phase, a few billion years after the Big Bang ($z \gtrsim 2$), galaxies evolve through in situ star formation enabled by the gases collapsed within dark matter halos. The abundant cold gases move toward the inner galaxy potential well and allow dominantly in situ star formation, increasing the mass of the inner galaxy more than that of the outer regions. Thus, in this phase, the total mass density profile slope, γ, steepens as the redshift decreases (i.e., $d\langle\gamma\rangle/dz > 0$).

In the second phase, at lower redshifts ($z \lesssim 1-2$), as the cool gas is exhausted and in situ star formation ceases, the dominant mode of evolution for massive ETGs is mass assembly via gas-poor (dry) mergers and dry accretion (Oser et al. 2010). Major dry mergers puff up the galaxy with a considerable increase in mass and size, resulting in a shallower radial density profile slope. Thus, γ shallows as redshift decreases (i.e., $d\langle\gamma\rangle/dz < 0$), such that the density profile tends to be isothermal (i.e., $\gamma = -2$, Blandford & Kochanek 1987) as $z \to 0$. On the other hand, in the same period, galaxies evolving via gas-rich processes tend to maintain a steeper density profile as the redshift decreases (Barnes & Hernquist 1991; Mihos & Hernquist 1994).

Current advanced cosmological simulations, e.g., Magneticum (Remus et al. 2017) and IllustrisTNG (Wang et al. 2019), which also incorporate models of stellar and active galactic nuclei (AGN) feedback are broadly consistent with the above galaxy evolution model. In particular, Magneticum and IllustrisTNG simulations predict that from $z = 2$ to 0, the density profile slope of ETGs shallows, from γ between -2.2 and -3.5 at $z \sim 2$ to $\gamma = -2$ as $z \to 0$.

Observational probes such as the dynamics of H I gas, globular clusters, planetary nebulae, and analysis of X-ray gas temperatures have found an average isothermal slope ($\gamma \sim -2$) for local ($z \sim 0$) ETGs (Weijmans et al. 2008; Brodie et al. 2014; Coccato et al. 2009; Humphrey & Buote 2010). Using the new 3D integral field spectroscopic observations with high-resolution 2D kinematics, Poci et al. (2017) and Derkenne et al. (2021, 2023) also found an average isothermal density profile for ETGs and suggested that γ does not evolve with redshift, i.e., $d\langle\gamma\rangle/dz \sim 0$ at $0 < z \lesssim 0.5$.

Most lensing observations so far have suggested either a slightly steeper slope than an isothermal density profile ($\gamma \sim -2.1$, Auger et al. 2010; Barnabè et al. 2011) or a gradual steepening of the slope with decreasing redshift (e.g., Bolton et al. 2012; Li et al. 2018a) for deflector ETGs. Therefore, regarding the evolution of density profile slope with redshift, lensing observations are apparently at conflict with simulations and marginally so with purely kinematic observations described in the above paragraphs. However, the $z \gtrsim 0.5$ end of the observed γ–z relation is still too sparsely populated to suggest a robust γ–z trend and requires a larger lens sample.

If true, the interpretation of most lensing observations so far suggests that massive ETGs instead require a gas-rich mass growth model, even at $z < 1$ (Sonnenfeld et al. 2014). However, this is contrary to the predictions from ETG evolution theories. A few studies have tried to address this problem. Remus et al. (2017) argue that the mismatch between simulations and lensing observations is artificial due to incorrect comparison. Etherington et al. (2023), however, suggest a mismatch among lensing observations due to the use of different lens modeling methods, "lensing-only" or "lensing and dynamical" (L&D), to measure the density profile slope. Thus, whether or not the conflict is real requires further detailed analysis.

This paper aims at populating the observed γ–z relation, especially at higher redshift ($\gtrsim$0.5), using deflector galaxies of seven galaxy-scale lenses from the `ASTRO 3D` Galaxy Evolution with Lenses (`AGEL`) survey (Tran et al. 2022, hereafter `AGEL`-DR1). Here we also try to understand the γ–z relation by comparing lensing observations, dynamical observations, and simulations.

The deflectors in our pilot lens sample of seven are all massive ETGs with redshifts in the range $0.3 < z < 0.9$; five of these galaxies are at $z \gtrsim 0.5$. To obtain the total mass density profile of deflectors, we model `AGEL` lenses using the "lensing-only" method with the advanced lens modeling software Gravitational Lens Efficient Explorer (GLEE, Suyu & Halkola 2010) in interactive mode. We further test the robustness of our lens mass model by comparing the directly measured stellar velocity dispersions ($\sigma_{\rm obs}$) of deflectors with their model-predicted velocity dispersions ($\sigma_{\rm pred}$).

Section 2 provides more details about the `AGEL` survey, the lens systems studied here, the images used for lens modeling, and the stellar velocity dispersion measurements. Section 3 describes the lens modeling process using GLEE. Section 4 presents our lens modeling results, comparison of $\sigma_{\rm pred}$ of deflector galaxies with $\sigma_{\rm obs}$, and the updated γ–z diagram. Section 5 discusses the evolution of γ with z obtained by simulations, purely dynamical observations, and lensing observations, as well as possible reasons behind discrepancies among these studies. In this section, we also compare the lensing-only density profile slopes with the slopes obtained via L&D analysis for our sample. Finally, Section 6 presents the conclusion of this work and further plans.

Cosmological constants for estimating distances and scales used in this paper are ΛCDM $H_0 = 70\ {\rm km\ s^{-1}\ Mpc^{-1}}$, $\Omega_{\rm m} = 0.3$, and $\Omega_{\rm vac} = 0.7$.

2. Data

The complete `AGEL` survey comprises about 1900 lens candidates (see Section 2.1.2 in AGEL-DR1) selected using convolutional neural networks from the Dark Energy Survey and Dark Energy Camera Legacy Survey. The `AGEL` survey has spectroscopically confirmed about 100 strong lenses, which include galaxy-scale, galaxy-group, and cluster-scale lens systems, with deflectors at $0 \lesssim z \lesssim 1$. Of the 100 confirmed lenses, redshifts for 53 are already published in AGEL-DR1, and the remaining lenses will be presented in `AGEL` Data Release 2 (DR2, in preparation).

To study galaxy evolution through the observed evolution of total mass profile with redshift (cosmic time), one needs galaxy-scale strong gravitational lenses where deflectors are single galaxies. About 50% of confirmed `AGEL` lens systems are galaxy-scale lenses, 50% of which already have high-resolution Hubble Space Telescope (HST) images. Of the

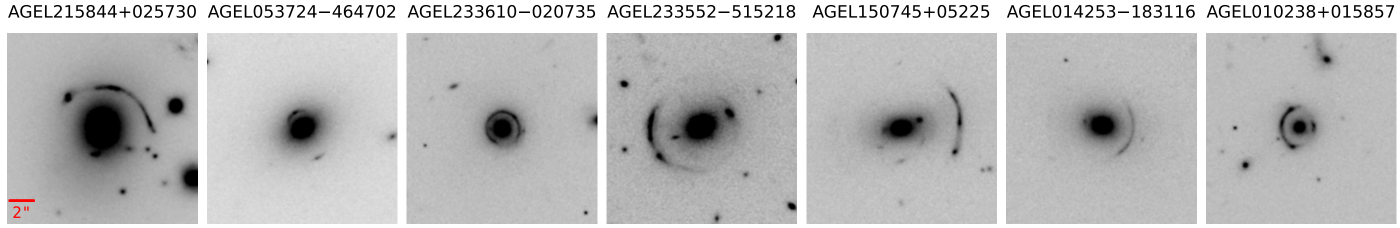

Figure 1. HST/WFC3 images of the seven AGEL lenses modeled here in the F140W filter. All seven images are 16″ × 16″ in size with a pixel resolution of 0.″08 pixel^{-1}. The red scale bar indicates a scale of 2″ that is the same for all images. Section 2 provides more details about the AGEL naming of these lens systems, deflector and background source redshifts, HST image observation programs, and the kinematic observations needed to test our lens modeling.

confirmed galaxy-scale lenses with HST imaging, we have 15 lens systems with deflectors at spectroscopic redshift $\gtrsim$0.5 and an additional 14 lenses with photometric redshift $\gtrsim$0.5. Follow-up observations are underway to obtain spectroscopic redshifts, HST images, and spectra for velocity dispersion measurements for more lenses.

Depending on the availability of (1) high-resolution HST images, (2) deflector and source spectroscopic redshifts, and (3) spectra for the deflector's stellar velocity dispersion measurements or velocity dispersion from the literature, we selected an initial sample of seven galaxy-scale lenses for this work. The first two are required for lens modeling and the velocity dispersion is required to check the robustness of our lens modeling results. The galaxy-scale AGEL lenses studied in this paper are AGEL 215844+025730 (hereafter AGEL 2158), AGEL 053724−464702 (hereafter AGEL 0537), AGEL 233610 −020735 (hereafter AGEL 2336), AGEL 233552−515218 (hereafter AGEL 2335), AGEL 150745+052256 (hereafter AGEL 1507), AGEL 014253−183116 (hereafter AGEL 0142), and AGEL 010238+015857 (hereafter AGEL 0102). Here, the numbers after "AGEL" comprise deflector galaxy coordinates, R.A. in hour:minute:second (hhmmss) and decl. in degree: minute:second (+/–ddmmss).

For lens modeling, we used the HST images taken by the Wide-Field Camera 3 (WFC3) in filter F140W from the SNAP programs #16773 (Cycle 29, P.I. K. Glazebrook) and #15867 (Cycle 27, P.I. X. Huang). The images are available at Mikulski Archive for Space Telescopes at the Space Telescope Science Institute and can be accessed via doi:10.17909/z66n-v326. Program #16773 observed the lens systems in the F140W filter for three exposures of 200 s (and also in the UVIS/F200LP filter for two exposures of 300 s). This multifilter observing sequence within one truncated HST orbit was optimized using LENSINGETC (Shajib et al. 2022a). Program #15867 observed the lens systems for three exposures of 399.23 s in the F140W filter. The data were reduced using the ASTRODRIZZLE software package from STScI (Avila et al. 2015). The drizzled pixel size in the F140W filter was set to 0.″08. The HST images of the seven AGEL lenses modeled in this paper are presented in Figure 1.

The deflector redshift ($z_{\rm defl}$), source redshift ($z_{\rm src}$), kiloparsec-to-arcsecond scale at the deflector plane, and line-of-sight stellar velocity dispersion ($\sigma_{\rm obs}$) of the deflector galaxy in our lens sample are provided in Table 1. Deflector redshifts for AGEL 2158, AGEL 2336, AGEL 1507, and AGEL 0102 are taken from the Baryon Oscillation Spectroscopic Survey (BOSS) of the Sloan Digital Sky Survey (SDSS-BOSS, Eisenstein et al. 2011). Source and deflector redshifts for the remaining lenses, except for AGEL 0537, are taken from AGEL-DR1. Redshifts for AGEL 0537 are measured by us using spectra obtained by the X-shooter spectrograph (Vernet et al. 2011) at the ESO Very Large Telescope (VLT).

The single-aperture line-of-sight stellar velocity dispersions, $\sigma_{\rm obs}$, for the deflector galaxies of AGEL 2158, AGEL 2336, and AGEL 1507 are taken from SDSS-BOSS measurements available in the literature (Thomas et al. 2013). For the remaining lenses, we measured each deflector's $\sigma_{\rm obs}$ from its absorption line spectrum with the help of the penalized pixel-fitting stellar kinematics extraction (PPXF, Cappellari 2012, 2023) software. For AGEL 0537, AGEL 2335, and AGEL 0142, deflector spectra were obtained using VLT/X-shooter. Spectra for AGEL 0102 were obtained using the Echellette Spectrograph and Imager (ESI, Sheinis et al. 2002) at the Keck II telescope. To measure the velocity dispersions using PPXF, we used templates from the medium-resolution Isaac Newton Telescope library of empirical spectra (MILES, Sánchez-Blázquez et al. 2006) and a 12th-order additive Legendre polynomial to correct low-frequency continuum variations and remove residuals resulting from minor flux calibration errors (following van de Sande et al. 2017). The seeing conditions for these observations, which are later required to predict velocity dispersions based on our lens modeling results, are listed in Table 1.

3. Lens Modeling

Gravitational lensing is the deflection of light coming from a background source by a foreground mass distribution that forms magnified and distorted images of the background source. In the case of strong lensing multiple images of the background source are observed. The foreground mass is usually referred to as the deflector or the lens. During lens modeling, we constrain the mass density profile of the deflector via the lens equation: $\boldsymbol{\beta} = \boldsymbol{\theta} - \alpha(\boldsymbol{\theta})$, and reconstruct the background source's intrinsic image. The lens equation links the lens plane (also known as the observed image plane) coordinates, $\boldsymbol{\theta}$, with those of the background source plane, $\boldsymbol{\beta}$, via the scaled deflection angle $\alpha(\boldsymbol{\theta})$ that is associated with the gradient of the lens potential $\alpha(\boldsymbol{\theta}) = \nabla\psi(\boldsymbol{\theta})$.

Essentially we measure the dimensionless surface (projected) lens mass density, also known as convergence, denoted by κ. Convergence is related to the lens potential via the Poisson equation $2\kappa = \nabla^2\psi(\boldsymbol{\theta})$. Generally, convergence is expressed in units of the critical density, $\Sigma_{\rm crit} = \frac{c^2 D_{\rm s}}{4\pi G D_{\rm d} D_{\rm ds}}$, of a lens system. Here, $D_{\rm s}$, $D_{\rm d}$, and $D_{\rm ds}$ are angular diameter distances between observer and source, observer and deflector, and deflector and source, respectively. The scaled deflection angle is related to the actual deflection angle, $\hat{\alpha}(\boldsymbol{\theta})$, via

Table 1
AGEL Pilot Lens Sample

Name (1)	$z_{\rm defl}$ (2)	$z_{\rm src}$ (3)	scale$_{\rm defl}$ (kpc/″) (4)	size$_{\rm im}$ (″) (5)	size$_{\rm src}$ (″) (6)	$\sigma_{\rm obs}$ (km s^{-1}) (7)	Aperture (″) (8)	Instrument (9)	Seeing (″) (10)	$\sigma_{\rm pred}$ (km s^{-1}) (11)	$\mathfrak{m}_{\rm ap,gals}$ (mag) (12)	$R_{\rm half,gal}$ (″) (13)	$\gamma^{\rm lens}$ (14)	$\gamma^{\rm L\&D}$ (15)
`AGEL` 2158	0.28654[a]	2.08015	4.319	11.2	1.83 × 2.04	322 ± 17	2	SDSS-BOSS	1.4	315 ± 19	16.11 ± 0.02	2.428 ± 0.087	1.820 ± 0.014	1.91 ± 0.03
`AGEL` 0537	0.35200	2.34430	4.940	7.04	0.63 × 0.72	288 ± 19	11 × 1.2	X-shooter	0.71	237 ± 7	17.17 ± 0.03	1.007 ± 0.050	1.810 ± 0.016	2.10 ± 0.05
`AGEL` 2336	0.49417[a]	2.66173	6.065	4.96	0.84 × 1.00	272 ± 35	2	SDSS-BOSS	1.4	285 ± 10	17.97 ± 0.04	0.687 ± 0.043	2.248 ± 0.042	2.20 ± 0.10
`AGEL` 2335	0.56600	2.22450	6.502	8.96	1.54 × 2.09	321 ± 27	11 × 1.2	X-shooter	0.85	426 ± 15	17.37 ± 0.08	1.984 ± 0.301	2.020 ± 0.018	1.78 ± 0.05
`AGEL` 1507	0.59454[a]	2.16275	6.654	11.2	1.41 × 1.16	303 ± 38	2	SDSS-BOSS	1.4	322 ± 27	17.70 ± 0.03	1.432 ± 0.060	1.620 ± 0.018	1.66 ± 0.07
`AGEL` 0142	0.63627	2.46972	6.868	8.00	1.46 × 1.60	316 ± 40	11 × 1.2	X-shooter	0.70	385 ± 29	17.59 ± 0.06	1.460 ± 0.165	2.208 ± 0.100	1.97 ± 0.10
`AGEL` 0102	0.86690[a]	1.81696	7.708	4.96	0.94 × 1.01	291 ± 51	20 × 1	ESI	0.8	339 ± 12	17.30 ± 0.05	0.981 ± 0.083	1.944 ± 0.028	1.72 ± 0.20

Note. Column (1): system name. Columns (2) and (3): deflector and source spectroscopic redshifts, respectively, all with a typical uncertainty of $\lesssim$0.00005. Column (4): kiloparsec-to-arcsecond scale for deflector plane. Column (5): image square grid cutout size. Column (6): source rectangular (length × width) grid cutout size. Column (7): directly measured stellar velocity dispersions of deflector galaxy. Columns (8) and (9): aperture size of the instruments used for $\sigma_{\rm obs}$: SDSS-BOSS with shell aperture of diameter 2″, X-shooter and ESI with rectangular slit aperture. Column (10): FWHM size of seeing disk for the spectroscopic observations used to measure the velocity dispersions. Column (11): stellar velocity dispersion of deflector predicted using LENSTRONOMY's GALKIN routine based upon our most probable lens models and assumed anisotropy (see Section 3.4). Columns (12) and (13): apparent magnitude of the deflector galaxy in the AB magnitude system and overall half-light radius of the deflector galaxy along the major axis, respectively, obtained by integrating the double Sérsic fits obtained during lens light modeling. Column (14): magnitude of the slope of the power-law mass density profile ($\rho \propto r^{-\gamma^{\rm lens}}$) for deflector galaxies obtained using lensing-only analysis. Column (15): magnitude of the slope of the power-law mass density profile for deflector galaxies obtained using joint lensing and dynamical analysis assuming isotropic stellar orbits.

[a] Taken from `BOSS` (Eisenstein et al. 2011).

$\alpha(\boldsymbol{\theta}) = D_{\mathrm{ds}}/D_{\mathrm{s}}\hat{\alpha}(\boldsymbol{\theta})$. See Schneider et al. (1992) for a detailed derivation of lensing equations from general relativity.

We used GLEE (Suyu & Halkola 2010; Suyu et al. 2012) for lens modeling, which involves modeling the total mass profile and the light profile of the deflector, and reconstructing the background source surface brightness. GLEE is an interactive modeling software that uses Bayesian optimization algorithms such as simulated annealing and Markov Chain Monte Carlo (MCMC) methods for parameter estimation (Kirkpatrick et al. 1983; Dunkley et al. 2005). GLEE is used for "lensing-only" lens modeling where we only need a high-resolution image to perform modeling in single-plane mode. Later, we require source and deflector redshifts to obtain the deflector mass profile from the unitless convergence profile. We also use additional kinematic information, such as the observed stellar velocity dispersion of the deflector galaxy, to check the accuracy of the deflector mass model. In the following sections, we describe the mass and light model parameterizations that we used, input data/files required, and the process of lens modeling with GLEE.

3.1. Model Parameters

To model the deflector's projected total mass density profile, we used the softened power-law elliptical mass distribution (SPEMD, Barkana 1998) along with an external shear component. In general, SPEMD profiles have a constant density within a core radius R_{c}, followed by an elliptically symmetric power-law fall-off. Parameters for the SPEMD profile based on the FASTELL code from Barkana (1998) are: centroid position in arcsec (x_m, y_m), mass axis ratio (q_m), mass position angle (φ_m in radians, measured counterclockwise from the positive x-axis), projected Einstein radius (R_{Eins} in arcseconds) along the major axis, the radial power-law slope ($-\gamma^{\mathrm{lens}}$), and the core radius R_c, set to 10^{-4} arcsec in this work.

Convergence, κ, for the SPEMD profile for a very small core radius, in the limit $\lim_{R_{\mathrm{c}}\to 0}\kappa(x, y)$, is expressed as

$$\kappa(x, y) = \frac{3 - \gamma^{\mathrm{lens}}}{1 + q_{\mathrm{m}}}\left[\frac{R_{\mathrm{Eins}}}{\sqrt{(x - x_m)^2 + \frac{(y - y_m)^2}{q_{\mathrm{m}}^2}}}\right]^{\gamma^{\mathrm{lens}} - 1}. \quad (1)$$

The mass distribution is rotated by the mass position angle φ_m during modeling. Here the parameter value $\gamma^{\mathrm{lens}} = 2$ corresponds to an isothermal three-dimensional mass density profile ($\rho \propto r^{-2}$). The spherical equivalent Einstein radius, θ_{Eins}, is related to R_{Eins} via $\theta_{\mathrm{Eins}} = (2/(1 + q_{\mathrm{m}}))^{1/(\gamma^{\mathrm{lens}} - 1)}\sqrt{q}_{\mathrm{m}} R_{\mathrm{Eins}}$ (see Suyu et al. 2013).

For point sources, the magnification (μ) due to lensing is dependent on the convergence and shear ($\gamma_{\mathrm{tot}}(\gamma_1, \gamma_2) = \sqrt{\gamma_1^2 + \gamma_2^2}$) caused by the deflector. It is given by the determinant of the magnification tensor ($\det(\mathbf{A}^{-1})$) as $\mu = \det(\mathbf{A}^{-1}) = 1/((1 - \kappa)^2 - \gamma_1^2 - \gamma_2^2)$. However, the magnification of an extended elliptical or irregular background source depends on the magnification matrix (κ, γ_{tot}) as well as the intrinsic surface brightness distribution of the background source, which is not already known (Treu 2010; Birrer 2021).

The additional external shear accounting for the tidal gravitational potential of the deflector's local environment is parameterized using the external shear magnitude (γ_{ext}) and position angle (φ_{ext}) measured anticlockwise from the positive x-axis. The lens potential associated with the external shear (taken from Suyu & Halkola 2010) can be expressed as

$$\psi_{\mathrm{ext}}(x, y) = \frac{1}{2}\gamma_{\mathrm{ext}}\{(x^2 + y^2)\cos(2\varphi_{\mathrm{ext}}) + 2xy\sin(2\varphi_{\mathrm{ext}})\}. \quad (2)$$

Here $\varphi_{\mathrm{ext}} = 0$ means the lensed image is stretched horizontally, and $\varphi_{\mathrm{ext}} = \pi/2$ means the image is stretched vertically.

To model the deflector's light profile, we use the Sérsic function (Sérsic 1963), which defines the apparent intensity at any point (x, y) at an elliptical isophote at radius $R(x, y) = \sqrt{(x - x_{\mathrm{L}})^2 + (y - y_{\mathrm{L}}/q_{\mathrm{L}})^2}$ from the light/photometric center (x_{L}, y_{L}) of a galaxy as

$$I(x, y) = A\exp\left\{-b_n\left[\left(\frac{R(x, y)}{R_{\mathrm{eff}}}\right)^{1/n} - 1\right]\right\}. \quad (3)$$

Here, q_{L} is the ratio of the galaxy's photometric minor and major axes, n is the Sérsic index representing profile shape, A is called the profile amplitude and represents the intensity at R_{eff}, and b_n is a Sérsic index-dependent normalization constant such that R_{eff} represents the half-light radius in the direction of the semimajor axis. The value of b_n is calculated by solving $\Gamma(2n) = 2\gamma(2n, b_n)$, where $\Gamma(2n)$ is the complete gamma function and $\gamma(2n, b_n)$ is the incomplete gamma function. It can also be approximated by $b_{\mathrm{n}} \approx 2n - 1/3 + 4/405n + 46/25{,}515n^2$ for $0.36 < n < 10$ (Ciotti & Bertin 1999; Dutton et al. 2011).

3.2. Input Files for Lens Modeling

Lens modeling with GLEE requires many input files such as the lens image cutout, the point-spread function (PSF) for the image, the arc mask, the lens/deflector mask, and the error map for the input lens image. Image cutout sizes ($\mathrm{size}_{\mathrm{im}}$) for our galaxy-scale lenses are mentioned in Table 1; these are about 4–5 times the galaxy half-light radius ($R_{\mathrm{half,gal}}$). The cutout sizes are selected to include lensed sources (Einstein radius $\lesssim 3''$–$4''$) and the immediate environment of the deflectors ($\lesssim 4''$–$6''$). We obtained the PSF for the HST images using TINYTIM (Krist et al. 2011).

The arc mask is a FITS file marking the pixels containing lensed source, e.g., arc plus counter-image, in the lens image cutout. The lens mask is a FITS file masking pixels containing the surrounding luminous objects, e.g., foreground stars, which are not a part of the deflector potential. We generated the masks manually by marking the mask regions using DS9 followed by conversion from region file to FITS file. Arc and lens masks are important to avoid light contamination from the lensed sources, foreground stars, and nearby bright galaxies when modeling the lens (deflector) surface brightness. The arc mask is further used to mark lensed background source regions required for source reconstruction.

We obtained the error maps by adding the background noise (σ_{bkg}) and the Poisson noise (σ_{P}) in quadrature for each pixel ($\sqrt{\sigma_{\mathrm{bkg}}^2 + \sigma_{\mathrm{P}}^2}$). Here, the background noise is the standard deviation calculated from an empty region of sky in the science image, and the Poisson noise for each pixel is the ratio of reduced image intensity (in counts per second) to exposure time ($\sigma_{\mathrm{P}} = \sqrt{\mathrm{intensity/exposure\ time}}$). A detailed description of these input files and their preparation can also be found in Ertl et al. (2023, Section 2.1.1).

3.3. Modeling with GLEE

Lens modeling using GLEE is performed in three phases. First, using the "position modeling," we obtain an initial guess for the lens mass (SPEMD) profile parameters. Second, we perform the lens light modeling, which is independent of the mass model. Third, we perform "extended source modeling," which involves lens mass modeling and source reconstruction. These three phases are described in detail below.

We assume uniform priors on the lens mass and light profile parameters. The parameters obtained from the first phase, position modeling, enable faster convergence than when using extended source modeling directly. However, the likelihood of the lens mass profile parameters from the position modeling phase is not included in the final likelihood during extended image modeling, which provides the final most probable lens mass model.

We use simulated annealing for parameter optimization during position modeling. However, for efficient sampling/optimization during lens light modeling and extended source modeling, we use the EMCEE ensemble sampler (Foreman-Mackey et al. 2013) and the Metropolis–Hastings (M–H) MCMC algorithm. The EMCEE routine, which is highly parallelizable, is used to obtain the first samples and first sampling covariance matrix. Subsequently, use of the M–H MCMC algorithm with the covariance matrix enables faster convergence, where convergence is tested by the power spectrum method from Dunkley et al. (2005).

3.3.1. Position Modeling with GLEE

Position modeling constrains the lens mass distribution parameters using the lensed image and source positions with respect to the deflector position (Halkola et al. 2006, 2008). We identify the positions of the multiple images of the background source (i.e., the centroid/photo peak) of the lensed galaxy or a bright star-forming clump) using DS9 visualization. Position modeling has two steps.

First, the lens equation ($\boldsymbol{\beta} = \boldsymbol{\theta} - \alpha(\boldsymbol{\theta})$) is used to predict the intrinsic source position ($\boldsymbol{\beta}$) using the observed multiple positions of the lensed source ($\boldsymbol{\theta}$) and the scaled deflection angle ($\alpha(\boldsymbol{\theta})$) based upon the prior deflector mass profile parameters. This maps the lensed image positions back to the source plane via the lens equation. Each lensed source position predicts an intrinsic source position, and the final intrinsic source position is taken as their magnification-weighted average. Further, the lens mass profile parameters (linked with the deflection angle as described in Section 3.1) are varied to minimize the source position $\chi^2_{\rm pos}$ defined in Halkola et al. (2006, their Equation (7)).

The second step optimizes deflector mass profile parameters using the observed image peak positions as constraints. Here, the lensed source positions are predicted based on the intrinsic source position and lens mass model obtained in the previous step. Further, the lens mass model parameters are varied to minimize image position $\chi^2_{\rm pos}$ (Halkola et al. 2006, their Equation (6)) based on the difference between the observed and predicted lensed source positions.

3.3.2. Lens Light Modeling with GLEE

Lens light modeling captures the deflector's surface brightness distribution by fitting one or more Sérsic functions directly to the image of the deflector galaxy (Equation (3)). This phase uses the arc and lens masks to block lensed source light and surrounding contaminants in the lens image cutout and captures only the deflector light.

We found that two Sérsic functions efficiently fit the deflector light in our galaxy-scale lenses, leaving behind a uniform residual. The most probable lens light model parameters are obtained by minimizing the lens surface brightness $\chi^2_{\rm SB}$ provided in Ertl et al. (2023, their Equation (5)). The lens light model obtained here is further used to separate the lens light overlapping with the arc in the next phase so that the arc light without contamination from the deflector can be used for source reconstruction. For the same reason, we mask out any other bright object near or overlapping with the arc.

3.3.3. Extended Source Modeling with GLEE

This phase involves constraining the lens mass profile and external shear by reconstructing the surface brightness profile of the background source (following Suyu et al. 2006; Suyu & Halkola 2010). Here, we improve upon the lens mass model obtained from the position modeling with the help of the multiply lensed surface brightness distribution of the extended background source, which offer tighter constraints on the mass model.

GLEE performs a pixellated source reconstruction on a grid of fixed pixel dimensions following conservation of surface brightness. The intrinsic source image is reconstructed via Bayesian regularized linear inversion of lensed source surface brightness. The regularization functions can be curvature or gradient depending on whether the lensed source is intrinsically smooth or clumpy. For all the lenses presented here, as the lensed sources appear to be featureless and smooth, we used the "curvature" regularization for reconstructing the source surface brightness distribution.

The source grid size (size$_{\rm src}$), mentioned in Table 1, is the minimal rectangular region on the source plane that contains the area to which the arc mask on the image plane maps (via the lens equation). The dimensions of the source grid are chosen such that the pixel resolution of the source is approximately that of the image divided by the square root of the average magnification (see Suyu et al. 2006).

The expression for the likelihood of the lens mass model parameters, which is equivalent to the Bayesian evidence of source reconstruction, is provided in Suyu & Halkola (2010, their Equation (12)). The best-fit or the most probable lens model is selected when the reduced chi-square ($\chi^2_{\rm red}$) for extended source reconstruction lies between 0.95 and 1.05. $\chi^2_{\rm red}$ is dependent on the Bayesian evidence of the source reconstruction, the likelihood of the lens light fitting, and the effective degree of freedom; it is calculated in GLEE following Suyu et al. (2006).

3.4. Model-predicted Stellar Velocity Dispersion

Lens modeling based solely on the imaging observables can have various degeneracies related to model parameterizations or intrinsic to data (see Shajib et al. 2022b). Importantly, the lens mass model is affected by the mass-sheet degeneracy (MSD). MSD is a result of a multiplicative transformation of the lens equation known as the mass-sheet transformation (MST, Falco et al. 1985), which can alter the mass distribution (e.g., κ map) without affecting the resultant lensed image configuration

(Schneider & Sluse 2013). MST also suggests the possibility of non-power-law mass models (see Birrer et al. 2020).

Only prior knowledge of the intrinsic size or intrinsic magnification of the source or an independent measure of lensing potential can break this degeneracy. Therefore, it is vital to check the modeling results using additional kinematic observations that can provide an independent measure of the lensing potential. One way to check the lens modeling results is by comparing the velocity dispersion predicted by the final lens model, $\sigma_{\rm pred}$, with the observed one, $\sigma_{\rm obs}$.

We used the GALKIN module of LENSTRONOMY (Birrer & Amara 2018; Birrer et al. 2021) software to obtain $\sigma_{\rm pred}$. GALKIN constrains $\sigma_{\rm pred}$ via spherical Jeans modeling with the help of the deflector's mass model, light profile, and stellar anisotropy for a given observing condition. While calculating $\sigma_{\rm pred}$ for a deflector galaxy, we used the same aperture size, aperture type, and FWHM size of the seeing disk as in the observing condition for $\sigma_{\rm obs}$. The aperture type (circular shell or rectangular slit), aperture size centered around the galaxy centroid, and the seeing FWHM for $\sigma_{\rm obs}$ of deflectors in our lens sample are presented in Table 1.

The anisotropy distribution of stellar orbits is degenerate with the mass distribution and is often referred to as the mass–anisotropy degeneracy (Binney & Mamon 1982). Thus, one has to assume an anisotropy distribution to predict the velocity dispersion. For our sample, we use the Osipkov–Merritt (Osipkov 1979; Merritt 1985) radial anisotropy distribution, parameterized as $\beta_{\rm ani} = r^2/(r_{\rm ani}^2 + r^2)$. Here, $r_{\rm ani}$ is the free parameter determining the degree of anisotropy. The choice of anisotropy is critical to the predicted stellar velocity dispersion because a higher anisotropy can result in an overestimated stellar velocity dispersion and vice versa (see Figure B.1 in Birrer et al. 2020).

Many observations suggest that massive elliptical galaxies are generally isotropic to mildly radially anisotropic at larger radii, suggesting $\beta_{\rm ani} \lesssim 0.3$ (Binney 1978; Kronawitter et al. 2000; Saglia et al. 2000; Chen et al. 2016). Relatively oblate rotating ellipticals or lenticular galaxies can be isotropic in their central regions; however, they become radially anisotropic beyond a certain radius such that $\beta_{\rm ani} \lesssim 0.5$ (Cappellari et al. 2007). We vary the anisotropy radius uniformly between 1 and 10 times the galaxy's spatial (3D) half-light radius $r_{\rm eff}$, which corresponds to $0.01 \lesssim \beta_{\rm ani}(r_{\rm eff}) \lesssim 0.5$, consistent with Koopmans et al. (2009) based upon 58 ETGs in the Sloan Lens ACS Survey sample (SLACS, Bolton et al. 2006).

4. Results

4.1. Lens Models Obtained with GLEE

Aiming to measure the total mass density profile for the deflectors in our lens sample, we modeled all seven AGEL lenses following the "lensing-only" method described in Section 3 such that $\chi^2_{\rm red}$ for the final best-fit model is between 0.95 and 1.05. As depicted in Figure 2 for AGEL 0142 and in Figure A1 of Appendix A for the remaining six lenses, we successfully reconstructed the observed lensing configuration and the background source surface brightness for all seven systems. In Figures 2 and A1, we show the observed HST image, the most probable lens model, normalized residual,[18] convergence map (κ) for the deflector SPEMD density profile, magnification model (μ), and the background source reconstruction. The first five panels in Figure 2 have the same grid size and pixel resolution (0.08 arcsec pixel^{-1}). The source grid in the bottom rightmost panel has a higher resolution (0.04 arcsec pixel^{-1}) dependent on the observed image resolution and magnification caused by the lens (Suyu et al. 2006).

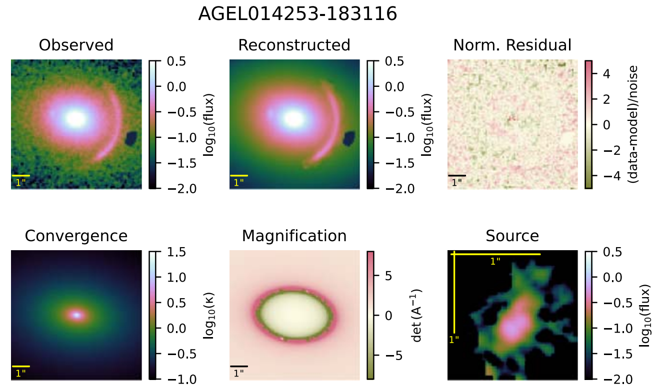

Figure 2. Lens modeling results for AGEL 0142 obtained using GLEE. Panels from top left to right represent the observed lens configuration, reconstructed lens model, and normalized residual. Panels from bottom left to right are convergence map of the deflector's density profile, magnification model, and the reconstructed background source. Here, flux is in units of electron counts per second, and convergence and magnification maps are unitless (described in Section 3). The black patches on the observed and reconstructed panels are pixels that are masked out during modeling. The yellow and black lines provide a scale of 1″ in the deflector and source planes. The angular sizes of the image and source grid are listed in Table 1.

Parameters for the deflector's convergence profile (Equation (1)), external shear (Equation (2)), and deflector's light profile (Equation (3)) are provided in Table A1. The subscripts 1 and 2 in Table A1 refer to the two Sérsic components of the deflector's light profile. All the parameter estimates are the median values of their one-dimensional posterior probability density function from the final MCMC chain. The uncertainties presented here are based on the 16th and 84th percentiles of the distribution, representing 68% (1σ) bounds around the median value.

We additionally measured the apparent magnitude ($\mathfrak{m}_{\rm ap,\,gal}$, in the HST F140W filter) and the projected half-light radius along the major axis ($R_{\rm half,gal}$) for the deflector galaxy in all seven lens systems (see Table 1). We obtained the total galaxy flux by integrating the two Sérsic components of the deflector's light profile over the image plane. Further, the flux in units of electron count per second (e^-/s) is converted to AB system magnitude following HST WFC3 Data Analysis. We numerically calculated the effective half-light radius along the major axis, $R_{\rm half,gal}$, of the deflector galaxy by integrating the two Sérsic components and looking for the major axis radius of the isophote enclosing half of the total galaxy flux. The equivalent circularized half-light radius, $R_{\rm half,gal,eq}$, is also presented in Table A1.

4.2. Comparing Model-predicted and Observed Velocity Dispersions

To check the accuracy of the deflector/lens mass density profile obtained via lens modeling, it is important to compare the model-predicted stellar velocity dispersion, $\sigma_{\rm pred}$, with the observed velocity dispersion $\sigma_{\rm obs}$. A significant difference between $\sigma_{\rm pred}$ and $\sigma_{\rm obs}$ may be an indication of an inappropriate

---

[18] The normalized residual for each pixel was obtained by dividing the difference between the observed image and the lens model by the estimated standard deviation.

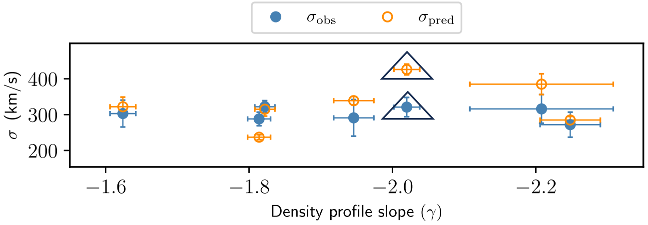

Figure 3. Observed (blue filled circles) and model-predicted (orange open circles) stellar velocity dispersions of deflector galaxies in the lens systems modeled in this paper, plotted against their total mass density profile slope ($\gamma = -\gamma^{\rm lens}$). For all lenses, except for AGEL 2335 marked by black triangles, $\sigma_{\rm pred}$ is consistent with $\sigma_{\rm obs}$ (see Section 4.2). Values of $\sigma_{\rm obs}$, $\sigma_{\rm pred}$, and $\gamma^{\rm lens}$ are provided in Table 1.

lens mass model due to parameter degeneracy (see Section 3.4), a potential line-of-sight mass overdensity (underdensity) if $\sigma_{\rm pred}$ is higher (lower) than $\sigma_{\rm obs}$ (Li et al. 2018b), or a possible deviation from the power-law mass model (Birrer et al. 2020). On the other hand, the consistency between $\sigma_{\rm obs}$ and $\sigma_{\rm pred}$ suggests that the lens models very well represent the actual mass distribution of deflector galaxies.

Following Section 3.4, we calculated $\sigma_{\rm pred}$ for deflector galaxies based on their most probable lens model parameters presented in Table A1. A plot comparing $\sigma_{\rm obs}$ and $\sigma_{\rm pred}$ against the slope of the total density profile of deflector galaxies is shown in Figure 3. Both $\sigma_{\rm obs}$ and $\sigma_{\rm pred}$ values for all lenses are provided in Table 1. For `AGEL` 2158, `AGEL` 2336, `AGEL` 1507, `AGEL` 0142, and `AGEL` 0102, the deflectors' observed stellar velocity dispersions are consistent with the model-predicted velocity dispersions within their 1σ uncertainty bounds. $\sigma_{\rm obs}$ and $\sigma_{\rm pred}$ for AGEL 0537 are consistent within the 2σ uncertainty bound of $\sigma_{\rm obs}$. Thus, the lens model obtained for the above systems conforms with their true mass distribution.

For `AGEL` 2335, $\sigma_{\rm pred} = 426 \pm 15$ km s^{-1} is much higher than the measured value $\sigma_{\rm obs} = 321 \pm 27$ km s^{-1}. In fact, $\sigma_{\rm pred}$ for `AGEL` 2335 is at the higher end of central velocity dispersions for ultramassive quiescent galaxies (e.g., Forrest et al. 2022). The reason behind the high $\sigma_{\rm pred}$ for `AGEL` 2335 may be linked with its large Einstein radius $R_{\rm Eins} = 3\overset{\prime\prime}{.}59$, which is more typical of a galaxy group than an individual galaxy.

In the DESI survey viewer, we find that the deflector galaxy in `AGEL` 2335 is the brightest among nearby galaxies at similar photometric redshift. Therefore, the deflector in `AGEL` 2335 may be a brightest cluster galaxy (BCG), and the cluster halo may be contributing to its large Einstein radius. Similarly, `AGEL` 0142, which also has a high $\sigma_{\rm pred} = 385 \pm 29$ km s^{-1}, may be a BCG or brightest group galaxy (BGG), although, for `AGEL` 0142, $\sigma_{\rm pred}$ is marginally consistent with $\sigma_{\rm obs} = 316 \pm 40$ km s^{-1} at the 1σ uncertainty level and $R_{\rm Eins} = 2\overset{\prime\prime}{.}33$ is typical of a galaxy-scale lens. We have encircled `AGEL` 2335 and `AGEL` 0142 deflectors in our γ–z diagrams discussed in the next section.

The cluster halo can affect the main deflector galaxy's density profile, including the slope parameter (Newman et al. 2015). Thus, when measuring the evolution of the density profile, the brightest cluster/group galaxy lenses should be distinguished from the isolated elliptical galaxy lenses based on their host halo mass. The BCGs and BGGs may be outliers or have a different γ–z trend compared with the isolated galaxies. Because our current sample is limited, we do not exclude the above two lenses; however, future studies with combined past and current lens samples and known lens environments will enable this investigation.

4.3. γ–z Diagram

Lens modeling provided us the slope parameter $\gamma = -\gamma^{\rm lens}$ for the total mass density profile of ETG deflectors in our lens sample by fitting a power-law density profile up to the Einstein radius. The best-fit $\gamma^{\rm lens}$ parameter along with 1σ uncertainty is provided in Table 1. Our deflector galaxy sample of seven has an average (lensing-only) density profile slope of $\langle\gamma\rangle = -1.95 \pm 0.09$ with an rms scatter of 0.21. Thus, the average slope of the density profile of deflector ETGs in our sample is consistent with an isothermal density profile ($\rho \propto r^{-2}$).

The distribution of density profile slope against redshift (and lookback time), the γ–z diagram, is shown in Figure 4. The `AGEL` deflectors are marked by blue stars. A linear ordinary least squares, OLS($\gamma|z$), regression over our lens sample provided a slope of $d\langle\gamma\rangle/dz = -0.2 \pm 0.2$ for the γ–z relation, which is consistent with γ not evolving with redshift. However, due to the small sample size, the fit parameters for the γ–z relation are statistically insignificant with a low Pearson correlation coefficient r-value of -0.2. Hence, we have not shown our line fit to the `AGEL` lenses in the γ–z diagram.

For comparison, in Figure 4 we also show the γ–z distribution/relation for ETGs obtained in past lensing observations, dynamical observations, and hydrodynamical simulations, namely, Magneticum, Horizon-AGN, and IllustrisTNG (from Remus et al. 2017; Peirani et al. 2019; Wang et al. 2019, respectively). The lensing observations are from Treu & Koopmans (2004), Auger et al. (2010), Barnabè et al. (2011), Ruff et al. (2011), Bolton et al. (2012), Sonnenfeld et al. (2013a), Li et al. (2018a), Etherington et al. (2023), and Tan et al. (2024). The dynamical observations are from Thomas et al. (2011), Poci et al. (2017), Bellstedt et al. (2018), Li et al. (2019), and Derkenne et al. (2021, 2023). Their markers are listed in the legend of Figure 4. A summary of specifications such as the method used to obtain the density profile, sample size, redshift range, radial range, change in γ with redshift ($d\langle\gamma\rangle/dz$), and the average slope ($\langle\gamma\rangle$) of the sample obtained in all above studies are provided in Table 2.

Upon analyzing the comprehensive γ–z diagram, shown in Figure 4, we note the following. Below $z < 0.5$, the distributions of γ for ETGs from individual observations (e.g., Auger et al. 2010; Bolton et al. 2012; Derkenne et al. 2021; Tan et al. 2024) and simulations roughly overlap with each other about the isothermal slope ($\gamma = -2$), although there is a significant scatter along the γ-axis. In comparison, at $z \gtrsim 0.5$ there are diverging trends suggesting increasing ($d\langle\gamma\rangle/dz > 0$), decreasing ($d\langle\gamma\rangle/dz < 0$), and constant ($d\langle\gamma\rangle/dz \sim 0$) growth of density profile slope with redshift. Horizon-AGN simulation and lensing observations from Bolton et al. (2012) and Li et al. (2018a) suggest $d\langle\gamma\rangle/dz > 0$. Magneticum simulation and lensing-only analyses from Etherington et al. (2023) and Tan et al. (2024) suggest $d\langle\gamma\rangle/dz < 0$. IllustrisTNG simulation and lensing observations from Treu & Koopmans (2004), Sonnenfeld et al. (2013b), and `AGEL` lenses suggest $d\langle\gamma\rangle/dz \sim 0$. This indicates apparent conflicts within and between simulations and observations, especially at $z \gtrsim 0.5$.

Establishing the observed γ–z trend, especially at $z \gtrsim 0.5$, is important to identify the physical processes responsible for galaxy growth by determining the simulations that best match

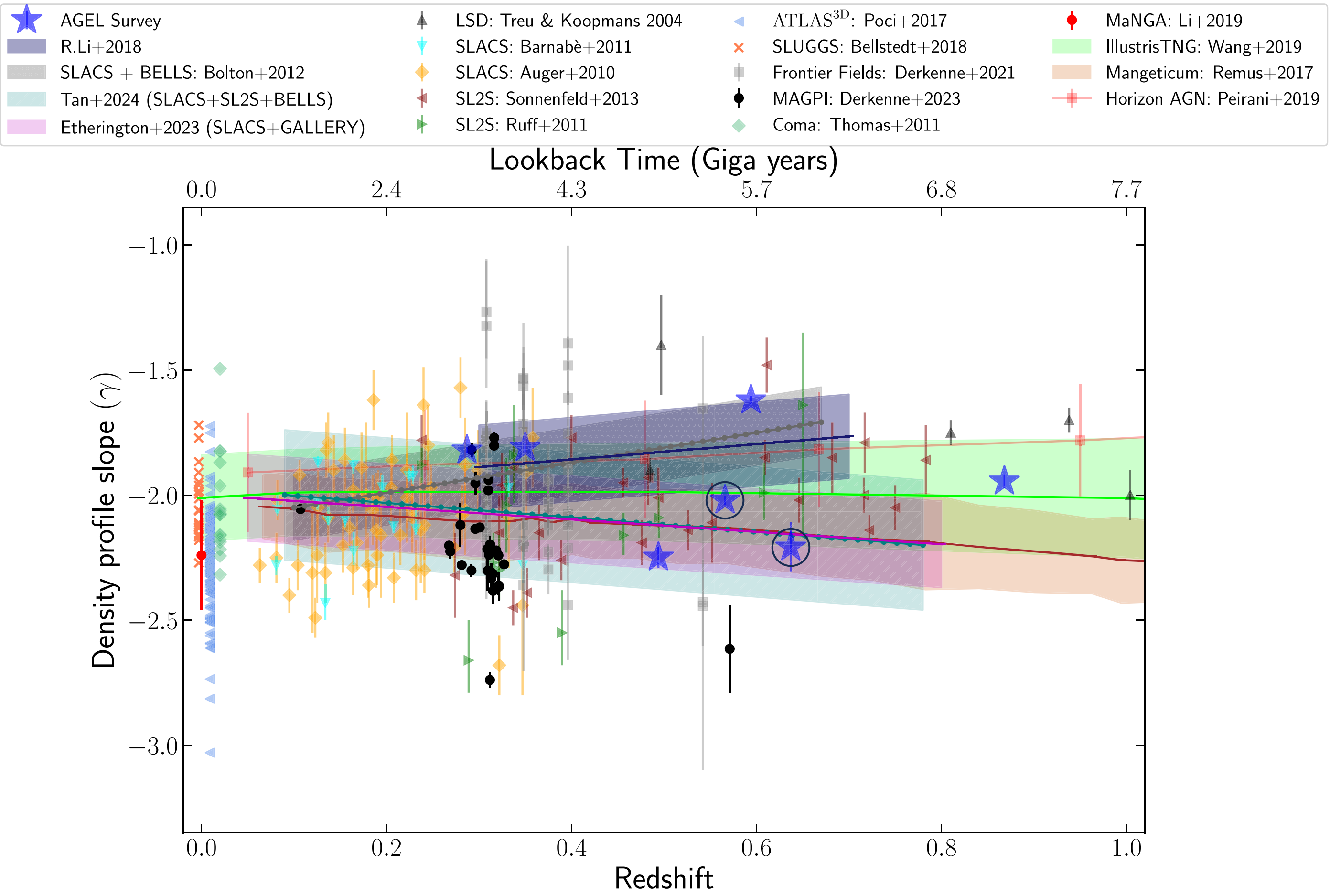

Figure 4. Distribution of total mass density power-law profile slope with redshift as seen using lensing observations, dynamical observations, and simulations. `AGEL` lenses modeled in this work are marked using blue stars. Encircled blue stars are the lenses `AGEL` 2335 and `AGEL` 1402 with high σ_{pred} (see Section 4.2). Markers for all the studies are explained in the legend and results from these studies are summarized in Table 2. All the shaded regions denote 68% population scatter about the corresponding best-fit relation. Overall, the γ–z diagram has a nonuniform distribution with redshift, such that there are more observed data points at $z \lesssim 0.5$ than at higher redshift. At $z \lesssim 0.5$, the γ vs. z distribution from lensing and dynamical observations overlaps well with that of simulations about the isothermal slope ($\gamma = -2$). However, at $z > 0.5$, the γ–z trends from simulations (red squares, green and brown shaded trends) and some lensing observations (see gray, blue, magenta, and teal shaded trends) seem to diverge. `AGEL` lenses with an average $\langle\gamma\rangle = -1.95 \pm 0.09$ and rms scatter of 0.21 are consistent with IllustrisTNG simulation; however, a larger lens sample is required to confirm the observed γ–z relation at higher redshift.

the observations. As discussed in the previous paragraph, the nature of the γ–z relation at $z \gtrsim 0.5$ is unclear. Also, there are fewer observed data points with increasing redshift due to observational challenges at $z \gtrsim 0.5$. Building on this work, the addition of galaxy-scale lenses, especially at $z \gtrsim 0.5$, available in the `AGEL` survey will help constrain the nature of the γ–z relation. Quadrupling the current sample will reduce the uncertainty on overall average density profile slope by a factor of two. Simultaneously, this will reduce the uncertainty in $\langle\gamma\rangle$ in each smaller redshift bin, thereby strengthening the measured γ–z relation.

Importantly, combining the quadrupled `AGEL` lens sample with the past lensing observations across various redshift ranges (see Table 2) can establish the γ–z relation. However, as Figure 4 shows and as is also discussed in the next section, there are discrepancies among observations as well; therefore, we need to understand and account for the differences in various studies before combining them. An alternative approach is to reanalyze the past lensing sample using the same method. As manual lens modeling is time-consuming, this will require automated modeling, e.g., Ertl et al. (2023) for quasar lenses, Etherington et al. (2023) and Tan et al. (2024) for galaxy–galaxy lenses. However, the precision of automated modeling may be lower than that of interactive modeling due to peculiarities in individual lenses.

5. Discussion

The lensing observations, dynamical observations, and simulations use different types of data and methods to measure density profiles. Here, we discuss the γ–z relations individually from lensing observations, dynamical observations, and simulations and possible reasons behind discrepancies between and within these categories. We have divided Figure 4 into the above three categories shown in Figures 5(a), (b), and (c), respectively. We have presented `AGEL` lenses modeled here in all three panels for comparison.

5.1. γ–z Relations from Lensing Observations

Even when comparing the same type of observations, it is essential to check whether their γ measurements represent the same property of the deflector mass density profile. Table 2 indicates these differences for lensing studies shown in Figure 5(a). There are two types of lensing observations:

Table 2
Details of Studies Presented in Figures 4 and 5

Study (1)	Method (2)	Sample Size (3)	Redshift (4)	$d\langle\gamma\rangle/dz$ (5)	$\langle\gamma\rangle_{\rm Sample}$ (6)	Radial Range (7)
This study	Lensing-only	7 (`AGEL`)	0.3–0.9	-0.2 ± 0.2	-1.95 ± 0.09	at $R_{\rm Eins}$
This study	L&D[a]	7 (`AGEL`)	0.3–0.9	0.47 ± 0.17	-1.91 ± 0.08	$\sigma_{\rm obs}$ aperture size
Treu & Koopmans (2004)	L&D	5 (LSD)	0.5–0.94	$\sim$0.0	-1.75 ± 0.1	$\leqslant R_{\rm eff}/8$
Auger et al. (2010)	L&D[a]	73 (SLACS)	0.06–0.36	$\sim$0.0	-2.08 ± 0.04	$\leqslant R_{\rm eff}/2$
Barnabè et al. (2011)	L&D	16 (SLACS)	0.08–0.33	$\sim$0.0	-2.07 ± 0.04	$\leqslant R^{\rm 3D}_{1/2}$
Ruff et al. (2011)	L&D[a]	11 (SL2S)	0.29–0.61	$\sim$0.0	-2.22 ± 0.19	$\leqslant R_{\rm eff}/2$
Ruff et al. (2011)	L&D	89 (SL2S, LSD, SLACS)	0.06–0.94	0.25 ± 0.11	-2.12 ± 0.04	$\leqslant R_{\rm eff}/2$
Bolton et al. (2012)	L&D[a]	79 (SLACS, BELLS)	0.1–0.6	0.60 ± 0.15	⋯	$\leqslant R_{\rm eff}$
Sonnenfeld et al. (2013b)	L&D	25 (SL2S)	0.2–0.8	0.10 ± 0.12	⋯	$\leqslant R_{\rm eff}/2$
Li et al. (2018a)	L&D	63 (BELLS, BELLS-GALLERY, SL2S)	0.3–0.7	0.31 ± 0.16	-2.00 ± 0.03	$\leqslant 1''$
Etherington et al. (2023)	Lensing-only[b]	48 (SLACS, GALLERY)	0.05–0.8	-0.25 ± 0.17	-2.08 ± 0.02	at $R_{\rm Eins}$
Tan et al. (2024)	Lensing-only[b]	77 (SLACS, SL2S, BELLS)	0.09–0.78	-0.29 ± 0.18	-2.05 ± 0.04	at $R_{\rm Eins}$
Thomas et al. (2011)	Dynamical	17 (Coma cluster)	0.0231	⋯	-2.00 ± 0.06	$0.1R_{\rm eff}$–$2R_{\rm eff}$
Poci et al. (2017)	Dynamical	150 (ATLAS$^{\rm 3D}$)	$\sim$0	⋯	-2.25 ± 0.02	$0.1R_{\rm eff}$–$2R_{\rm eff}$
Bellstedt et al. (2018)	Dynamical	22 (SLUGGS)	$\sim$0	⋯	-2.06 ± 0.04	$0.1R_{\rm eff}$–$2R_{\rm eff}$
Li et al. (2019)	Dynamical	2110 (MaNGA)	$\sim$0	⋯	-2.22 ± 0.01	$<R_{\rm eff}$
Derkenne et al. (2021)	Dynamical	64 (Frontier Fields cluster)	0.29–0.55	⋯	-2.01 ± 0.04	$0.1R_{\rm eff}$–$2R_{\rm eff}$
Derkenne et al. (2023)	Dynamical	28 (MAGPI)	$\sim$0.31	⋯	-2.22 ± 0.05	$0.1R_{\rm eff}$–$2R_{\rm eff}$
Remus et al. (2017)	Simulation	Magneticum	0-1	-0.21	-2.13 ± 0.15	$0.4R^{\rm 3D}_{1/2}$–$4R^{\rm 3D}_{1/2}$
Peirani et al. (2019)	Simulation	Horizon-AGN	0-1	>0	-1.85 ± 0.23	$0.5R_{\rm eff}$–$R_{\rm eff}$
Wang et al. (2019)	Simulation	IllustrisTNG	0-1	$\sim$0.0	-2.00 ± 0.19	$0.4R^{\rm 3D}_{1/2}$–$4R^{\rm 3D}_{1/2}$

Notes. Column (1): name of the study. Column (2): method used to constrain the total mass density profile of the galaxy. Column (3): sample size and the data survey. Column (4): redshift range of the deflectors/galaxies in the sample. Column (5): measured evolution of density profile slope with redshift (note that we represent the density profile as $\rho \propto r^{\gamma}$ with $\gamma < 0$ in this paper). The trends from Ruff et al. (2011), Li et al. (2018), and Tan et al. (2024) are $\partial\langle\gamma\rangle/\partial z$. Column (6): average density profile slope of the sample. Column (7): radial range over which slope (γ) was measured; for L&D analysis this represents the aperture of $\sigma_{\rm obs}$ used. Abbreviations for various data surveys are LSD—Lenses Structure and Dynamics (Koopmans & Treu 2004), SLACS—Sloan Lens ACS Survey (Bolton et al. 2006), BELLS—BOSS Emission-Line Lens Survey (Brownstein et al. 2012), GALLERY—Galaxy-Lyα Emitter Systems Survey (Shu et al. 2016), SL2S—Strong Lensing Legacy Survey (Cabanac et al. 2007), MAGPI—Middle Ages Galaxy Properties with Integral Field Spectroscopy (Foster et al. 2021), MaNGA—Mapping Nearby Galaxies at Apache Point Observatory (Bundy et al. 2015), SLUGGS—SAGES Legacy Unifying Globulars and Galaxies Survey (Brodie et al. 2014). The radius $R^{\rm 3D}_{1/2}$ represents the (three-dimensional) half-mass radius.

[a] Assumed isotropic orbits during Jeans modeling to constrain γ using $\sigma_{\rm obs}$.

[b] Etherington et al. (2023) and Tan et al. (2024) used automated modeling.

"lensing-only" and joint "lensing and dynamical" (L&D) analysis.

The "lensing-only" method, described in Section 3, mainly requires a high-resolution lens image and directly fits a power-law mass model to the lens configuration up to $R_{\rm Eins}$ via the lens equation. This method provides us with complete lensing information, including the constant power-law slope, γ, which is sensitive to the local slope at $R_{\rm Eins}$ (see Treu 2010). The lens model posterior from this method can be affected by MSD (Section 3.4), so it is essential to test the model's predicted velocity dispersion against the observed one. In Figure 5(a), this method is only used in Etherington et al. (2023, shown by magenta line), Tan et al. (2024, shown by teal dotted line), and this work for the `AGEL` lenses marked by blue stars.

L&D analysis uses the lens image only to obtain $R_{\rm Eins}$ and the deflector's light profile, and requires source and deflector redshifts to measure projected mass enclosed within $R_{\rm Eins}$. It further constrains the spherical power-law density profile using independently measured stellar velocity dispersion and assumed stellar anisotropy through spherical Jeans modeling (e.g., Koopmans et al. 2006). The choice of anisotropy affects the inferred density profile, and a telescope-time-expensive resolved kinematics is required to remove associated systematics (Cappellari 2016; Shajib et al. 2023). The L&D method essentially provides a global mass-weighted density profile slope within the radial range of $\sigma_{\rm obs}$ measurement (see Dutton & Treu 2014), and it is a good proxy for average slope within $R_{\rm eff}$ (Sonnenfeld et al. 2013b).

For a comparison, we also applied the L&D method assuming the same power-law model (Equation (1)) as used for lensing-only analysis for our sample. We used the Einstein radius and lens light profile already measured in our modeling process and used $\sigma_{\rm obs}$ to constrain the L&D slopes ($\gamma^{\rm L\&D}$) by solving the spherical Jeans equation using the LENSTRONOMY GALKIN routine (see Section 3.4). We considered simple isotropic orbits for our ETG lenses for this test.

We find a sample average of $\langle\gamma^{\rm L\&D}\rangle = -1.91 \pm 0.08$ with an rms scatter of 0.19, which is consistent with lensing-only measurements (cf. $\langle\gamma\rangle = -1.95 \pm 0.09$, scatter = 0.21) within the 1σ uncertainty level. L&D slopes for individual lenses are provided in Table 1. A one-to-one comparison between L&D and lensing-only slopes is provided in Appendix Figure B1. We find that the two types of slopes relate as $\gamma^{\rm L\&D} = (0.81 \pm 0.12)(\gamma^{\rm lensing-only} + 2) - (1.94 \pm 0.07)$ with a moderate Pearson coefficient (r-value) of 0.55. Here, the intercept -1.94 ± 0.07 represents the mean value and scatter of $\gamma^{\rm L\&D}$ at the reference lensing-only slope $\gamma^{\rm lensing-only} = -2$.

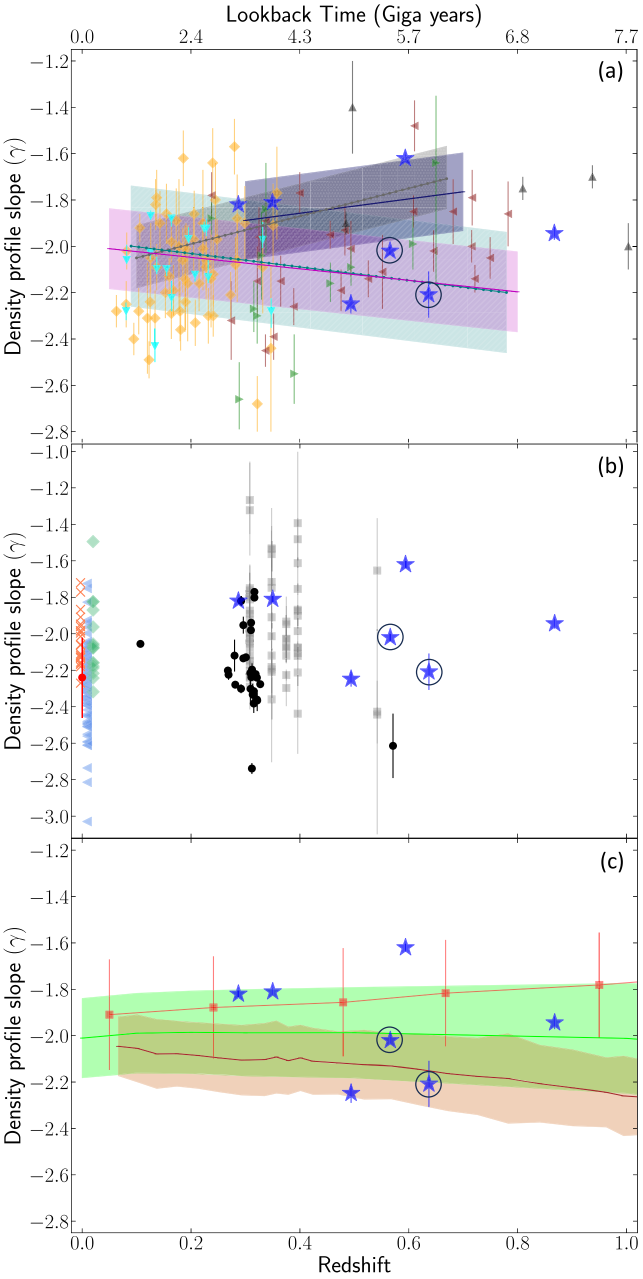

Figure 5. A breakdown of the γ–z diagram into the results from lensing observations (a), dynamical observations (b), and simulations (c). The AGEL lens sample modeled here is shown in all three panels for comparison with simulations and dynamical observations. Markers are the same as in Figure 4.

A γ versus z plot with L&D slopes for the AGEL sample is shown in Appendix Figure B2. Interestingly, with redshift, L&D slopes correlate as $\gamma^{\rm L\&D} = (0.47 \pm 0.17)(z - 0.57) - (1.89 \pm 0.06)$ with Pearson r-value of 0.53. This is consistent with past L&D observations but contrary to recent lensing-only observations (Etherington et al. 2023; Tan et al. 2024), whereas our lensing-only measurements suggest no slope evolution with $d\gamma/dz$ consistent with zero (see Table 2). Nonetheless, we emphasize the need to use a larger sample in the future to test the above correlations.

If the assumption of the power-law mass model is correct, there should be no discrepancies between lensing-only and L&D methods except if there are systematics in $\sigma_{\rm obs}$ measurement or the anisotropy assumption used in the L&D analysis. These two factors can bias the γ values and add scatter in the γ–z distribution (Xu et al. 2017; Birrer et al. 2020). On the other hand, the lensing-only and L&D methods will provide different slope values if the actual density profile is more complex than a simple power law. Either or both of the above could be a reason why the lensing-only γ–z trends from Etherington et al. (2023); Tan et al. (2024), and this work are different from those in L&D studies, e.g., Bolton et al. (2012, gray line) and Li et al. (2018a, navy-blue line).

Etherington et al. (2023) also find a higher scatter in γ measured via the lensing-only method than the L&D method for the same lens sample. They argue that $R_{\rm Eins}$ is close to an inflection point beyond which dark matter starts to dominate the baryonic matter, and the total density profile deviates from the power law. They suggest that the lensing-only measurements are therefore sensitive to the location of the inflection point, enhancing rms scatter in the measured slopes. L&D slopes, on the other hand, are averaged over an extended radial range, resulting in a smaller population scatter. If true, this could be behind the higher population scatter about the γ–z trend from Tan et al. (2024, scatter = 0.26) compared to past L&D studies (Bolton et al. 2012, scatter = 0.14).

In case the true mass model is not a power law, the difference in the radial range over which slope is weighted in the L&D observations or the difference in the aperture of $\sigma_{\rm obs}$ can produce different γ values even for the same lens. Thus, the use of different radial ranges in the past L&D observations (e.g., see Auger et al. 2010; Bolton et al. 2012; Li et al. 2018a) may be why their distributions do not align well and add a significant scatter in the γ–z diagram. Some studies are testing the possibility of a flexible non-power-law lens mass model (e.g., Birrer et al. 2020; Kochanek 2020; Shajib et al. 2021). For example, for future studies with a complete sample, Tan et al. (2024) suggest using a composite mass model with dark and baryonic matter modeled separately in the L&D analysis to obtain the total density profile for a better comparison with simulations.

5.2. γ–z Relations from 2D Dynamical Observations

Many 2D dynamical studies were restricted to local ETGs at $z \sim 0$ some years ago (e.g., Poci et al. 2017; Bellstedt et al. 2018; Li et al. 2019; Thomas et al. 2011, as shown in Figure 5(b)). Improved instrumentation is now pushing the resolved kinematic observation limit to intermediate redshifts $0.3 \lesssim z < 0.55$, such as Derkenne et al. (2021, black circles) and Derkenne et al. (2023, gray squares), shown in Figure 5(b).

Using 2D stellar kinematics and high-resolution HST images, dynamical observations measure the spatial total density profile via stellar dynamical (Jeans Anisotropic Multi-Gaussian Expansion or Schwarzschild) modeling with unconstrained anisotropy and inclination angle. These studies calculate γ as the mean logarithmic slope ($\Delta \log \rho / \Delta \log r$) over a certain radial range. Thus, using different radial ranges will produce different mean logarithmic slope values if the galaxy's total mass profile is not a power law with a constant slope.

Derkenne et al. (2023) dynamically measured the mean logarithmic slope of the density profile over the same radial range of $0.1R_{\rm eff}$–$2R_{\rm eff}$ for 28 MAGPI survey galaxies. Past dynamical studies have used variable radial ranges to measure γ. Therefore, for better comparison, Derkenne et al. (2023) recalculated slopes for the past ETG sample, except for Li et al. (2019), using the same radial range $0.1R_{\rm eff}$–$2R_{\rm eff}$. Figures 4 and 5 show the updated slopes for the dynamical sample.

As summarized in Table 2, the sample average density profile slopes obtained in dynamical studies at $z \sim 0$ and $0.3 < z < 0.55$ are close to the isothermal slope; therefore, Derkenne et al. (2021, 2023) suggest an overall lack of evolution (i.e., $d\langle\gamma\rangle/dz \sim 0$) of the mass density profile slope with redshift for ETGs. However, this conclusion requires further investigation because there is still a lack of resolved kinematic data at $0 < z < 0.3$ (see Figure 5(b)), and slope measurements for some dynamical samples have very high uncertainty (e.g., 0.2–0.6 in Derkenne et al. 2021).

The lack of dynamical observations at $0 < z < 0.3$ is supplemented by the SLACS lens sample, for which Auger et al. (2010) and Bolton et al. (2012) find a shallower sample average slope (2.08 ± 0.04) using the L&D method than the ATLAS^{3D}, MaNGA, and MAGPI dynamical observations ($\langle\gamma\rangle \sim -2.23 \pm 0.02$). This could be due to slopes weighted/averaged over different radial ranges (see Table 2) for possible density profiles with varying slopes.

The difficulty in acquiring spatially resolved kinematics at high redshifts significantly contributes to the large uncertainties in the dynamical slope measurements. This is where `AGEL` lenses are highly complementary and can provide measurements of total density profile slope for galaxy lenses at high z only using high-quality photometric lens images. In the future, a side-by-side comparison by applying lensing and 2D dynamical analysis on the same data set will be insightful for combining results from two types of observations to refine the γ–z relation.

5.3. γ–z *Relations from Simulations*

Comparison with observations confirms the simulation results and lets us understand galaxy evolution processes in more detail than observationally possible. Figure 5(c) shows that Magneticum, IllustrisTNG, and Horizon-AGN simulations suggest different evolutions of ETG density profile slope, γ, with redshift at $z \lesssim 1$. Though at $z \lesssim 0.5$ the γ–z relations from Magneticum and Horizon-AGN simulation seem to overlap well with the IllustrisTNG simulation ($\gamma \sim -2$) within their 1σ scatter bounds, all three simulated trends diverge as we move toward higher redshift.

Figures 4 and 5 represent the simulated γ–z relation only until $z = 1$ because the observational data are limited to $z \sim 1$. Magneticum simulation found a monotonic shallowing of γ for ETGs with decreasing redshift, starting from $\gamma \sim -3$ at $z \sim 2$ to $\gamma \sim -2$ at $z \sim 0$ (Remus et al. 2017). In contrast, Horizon-AGN simulation found a continuous steepening of γ with decreasing redshift, starting from $\gamma \sim -1.6$ at $z = 2$ to $\gamma \sim -2$ at $z \sim 0$ (Peirani et al. 2019). IllustrisTNG simulation, on the other hand, found a multiphase γ–z trend for ETGs (Wang et al. 2019). IllustrisTNG simulation found that, for galaxies in the main progenitor branch, γ steepens up to -2.2 during $2 < z < 4$ due to gas-rich evolution, then shallows to $\gamma \sim -2$ during $1 < z < 2$ mainly due to AGN feedback and then the isothermal slope ($\gamma \sim -2$) is maintained with a passive gas-poor evolution at $z \lesssim 1$.

The reason behind different γ–z simulation trends could be different models for galaxy evolution processes, e.g., baryonic versus dark matter interactions, gas cooling, subgrid physics, stellar feedback, or AGN feedback, adopted in simulations (Peirani et al. 2019; Wang et al. 2020; Mukherjee et al. 2021). Additionally, the discrepancy between simulations and lensing observations may be due to challenges in comparing the two. One challenge is due to methodological differences (Remus et al. 2017), e.g., the use of spatial (3D) radius in simulations rather than projected radius as in lensing observations when calculating γ (see Table 2). Second, simulations can track the evolution of the same galaxy sample over cosmic time, which is impractical for observations. Filipp et al. (2023) present an approach for direct comparison between observations and simulations by identifying direct counterparts of galaxies in both. However, the current sample of lenses needs to be expanded to apply their strategy.

The lensing-only average $\langle\gamma\rangle = -1.95 \pm 0.09$ and $d\langle\gamma\rangle/dz = -0.2 \pm 0.2$ for the `AGEL` sample modeled in this work seems consistent with the IllustrisTNG simulation with $d\langle\gamma\rangle/dz \sim 0$ at $z \lesssim 1$. However, it is not consistent with other simulations and some observations that suggest $d\langle\gamma\rangle/dz > 0$ (e.g., Li et al. 2018a; Bolton et al. 2012, Horizon-AGN) or $d\langle\gamma\rangle/dz < 0$ (e.g., Etherington et al. 2023, Magneticum). On the other hand, the L&D analysis results for `the AGEL` sample ($\langle\gamma\rangle = -1.91 \pm 0.08$ and $d\langle\gamma\rangle/dz = 0.47 \pm 0.17$) are consistent with the past L&D observations and Horizon-AGN simulation with $d\langle\gamma\rangle/dz > 0$. Distinguishing which simulation is favored by observations is possible only after establishing the observed γ–z trend at $z \gtrsim 0.5$ and accounting for possible methodological differences among observations and simulations. In future studies, the addition of high-z `AGEL` lenses and, further, careful combination with past lensing observations, e.g., SL2S (Sonnenfeld et al. 2013b, $0.2 \lesssim z \lesssim 0.8$), BELLS (Brownstein et al. 2012, $0.4 \lesssim z \lesssim 0.7$), and BELLS-GALLERY (Shu et al. 2016, $0.4 \lesssim z \lesssim 0.7$) samples, can help constrain the nature of the γ–z relation at $z \gtrsim 0.5$.

6. Conclusion

The observed evolution of galaxy density profiles with cosmic time is a critical test of theoretical models for galaxy evolution. However, density profiles are increasingly challenging to measure at higher redshifts. Here, we measure the relation between total matter density profile slope (γ) and redshift (z) using strong gravitational lenses at $z_{\rm defl} > 0.3$, which complements the dynamical observations at lower redshifts. In the γ–z diagram, we add seven new galaxy-scale lenses with $0.3 < z_{\rm defl} < 0.9$ from the `AGEL` survey (Section 2). We also investigate the apparent conflict between lensing observations, purely dynamical observations, and simulations in the γ–z diagram.

To obtain the total mass density profile of deflector galaxies, we perform lensing-only modeling using high-resolution HST images. We use state-of-the-art lens modeling software GLEE and assume a power-law mass profile with a constant slope for deflector galaxies (Section 3). To provide an independent test of our lens mass models, we also measured the stellar velocity dispersion, $\sigma_{\rm obs}$, for deflectors in four lenses and obtained $\sigma_{\rm obs}$ for the remaining three lenses from the SDSS-BOSS survey (Thomas et al. 2013).

We successfully reconstruct the lensing configuration and the background source surface brightness for all seven lenses (see Figures 2 and A1). Similar to existing studies, all of the seven deflectors in our pilot sample are ETGs. We find that the velocity dispersions, $\sigma_{\rm pred}$, predicted by our lens model for the deflector ETGs are consistent with the observed velocity dispersions, suggesting that our lens models are accurate, for all lenses except for `AGEL` 2335 (Section 4). The deflectors in `AGEL` 2335 and `AGEL` 0142 are likely to be brightest cluster/group galaxies and both have high $\sigma_{\rm pred}$ due to the cluster halo contributing to the lensing potential. We suggest future studies with a larger sample to separate the brightest cluster/group galaxies from isolated galaxies when studying the evolution of total density profile.

The deflector galaxies in our pilot lens sample have an average lensing-only density profile slope of -1.95 ± 0.09 with an rms scatter of 0.21, consistent with an isothermal density profile. The γ–z distribution of our sample with $d\langle\gamma\rangle/dz = -0.2 \pm 0.2$ is broadly consistent with the IllustrisTNG simulation (Wang et al. 2019), dynamical observations (Derkenne et al. 2021, 2023), and some lensing observations (Treu & Koopmans 2004; Sonnenfeld et al. 2013b), which suggest no slope evolution with redshift (Section 4). The lack of evolution in γ at $z \lesssim 1$ is consistent with the predictions of ETGs passively evolving through gas-poor mergers and maintaining a shallow isothermal ($\gamma = -2$) density profile (Wang et al. 2019). However, we need a larger statistical sample to confirm our findings.

We also present density profile slopes measured using the joint lensing and dynamical analysis. The L&D method, assuming isotropic stellar orbits, provides a sample average slope of -1.91 ± 0.08 with an rms scatter of 0.19, consistent with our lensing-only analysis. Regarding evolution with redshift, the L&D slopes tend to steepen with decreasing redshift, consistent with some past L&D observations (Bolton et al. 2012; Li et al. 2018a) but contrary to recent lensing-only observations (Etherington et al. 2023; Tan et al. 2024). This finding requires further detailed testing with varying anisotropy and a larger lens sample.

In the updated γ–z diagram, apart from differences between observations and simulations, we notice differences within observations (e.g., Bolton et al. 2012; Etherington et al. 2023) and within simulations (Section 5). Based on our comparisons, the possible reasons for the apparent discrepancies are a combination of the following: (1) systematics in the assumed anisotropy profile or $\sigma_{\rm obs}$ used in the L&D and purely dynamical modeling; (2) simplistic assumption of a power-law mass profile; and (3) challenges in comparing observations with the simulations. If the assumed power-law mass profile is inaccurate, then using different methodologies such as lensing-only and L&D to obtain the density profile or different radial ranges over which γ is averaged will provide different values. The differences between simulations are mainly due to the different physical processes adopted, such as the strength of AGN feedback (Peirani et al. 2019).

Building on the analysis in this paper, we plan to quadruple the modeled `AGEL` lens sample available from the `AGEL` survey, especially at $z > 0.5$, in a follow-up paper. This will help constrain the nature of the γ–z relation at the high-redshift end by reducing uncertainty in $\langle\gamma\rangle$ by a factor of two. Moreover, by combining our sample with past lensing observations after accounting for differences in the methodology, we can refine the γ–z relation even further. We will use the expanded sample to simultaneously investigate the evolution in associated galaxy properties (e.g., size, mass, kinematics, and stellar mass density) with cosmic time, which will provide improved tests for galaxy evolution models.

Acknowledgments

This research was supported by the Australian Research Council Centre of Excellence for All Sky Astrophysics in 3 Dimensions (ASTRO 3D), through project number CE170100013. The authors thank Yiping Shu for valuable feedback on this manuscript. The authors thank Alessandro Sonnenfeld for suggestions regarding joint lensing and dynamical analysis. The authors also thank the anonymous referee for constructive comments that improved the clarity of this paper. S.H.S. and S.E. thank the Max Planck Society for support through the Max Planck Research Group and Max Planck Fellowship for S.H.S. A.J.S. was supported by NASA through the NASA Hubble Fellowship grant HST-HF2-51492 from the Space Telescope Science Institute, which is operated by the Association of Universities for Research in Astronomy, Inc., for NASA, under contract NAS5-26555. T.J. and K.V.G.C. gratefully acknowledge financial support from NASA through grant HST-GO-16773, the Gordon and Betty Moore Foundation through Grant GBMF8549, the National Science Foundation through grant AST-2108515, and from a Dean's Faculty Fellowship. S.M.S. acknowledges funding from the Australian Research Council (DE220100003). S.L. acknowledges support by FONDECYT grant 1231187.

Software: NUMPY (Harris et al. 2020), SCIPY (Virtanen et al. 2020), ASTROPY (Astropy Collaboration et al. 2013, 2018, 2022), MATPLOTLIB (Hunter 2007), MULTIPROCESS (McKerns et al. 2012).

Appendix A
Lens Modeling Results

Table A1 provides the model parameters for the SPEMD density profile, external shear component, and light profile parameters captured using two Sérsic functions for the deflector galaxies in `AGEL` lenses modeled here. Furthermore, we also provide parameters for a single Sérsic fit for the lens light. However, the single Sérsic fit does not properly capture the total galaxy light, especially the central light; hence, the parameter $R_{\rm eff}$ obtained from the single Sérsic fit does not represent the actual half-light radius of the lens galaxy. The modeling procedure can be found in Section 3. Galaxy apparent magnitude in the HST/F140W band (AB mag) obtained by integrating the flux captured by two Sérsic components and the overall galaxy half-light radii $R_{\rm half,\ gal}$ along the semimajor axis for the deflector galaxies are already presented in Table 1. The circularized half-light radius, $R_{\rm half,gal,eq}$, obtained via $R_{\rm half,gal,eq} = R_{\rm half,\ gal}\sqrt{q_{\rm L}}$ (see Ciambur 2016) is also provided in Table A1.

Figure A1 shows the most probable lens model of the remaining six lenses: `AGEL` 2158, `AGEL` 0537, `AGEL` 2336, `AGEL` 2335, `AGEL` 1507, and `AGEL` 0102. From left to right, each panel in Figure A1 shows the observed HST image, predicted model of the lens system, normalized residual, convergence map, magnification model, and the reconstructed source. Here, flux is in units of electron count per second. The first five panels are in the deflector plane. The rightmost panel is in the source plane. The first five panels have the same grid size and pixel resolution; however, the source grid in the rightmost panel has a higher resolution that depends on the observed image resolution and magnification caused by the lens. The angular sizes for the lens images and background source grid are provided in Table 1.

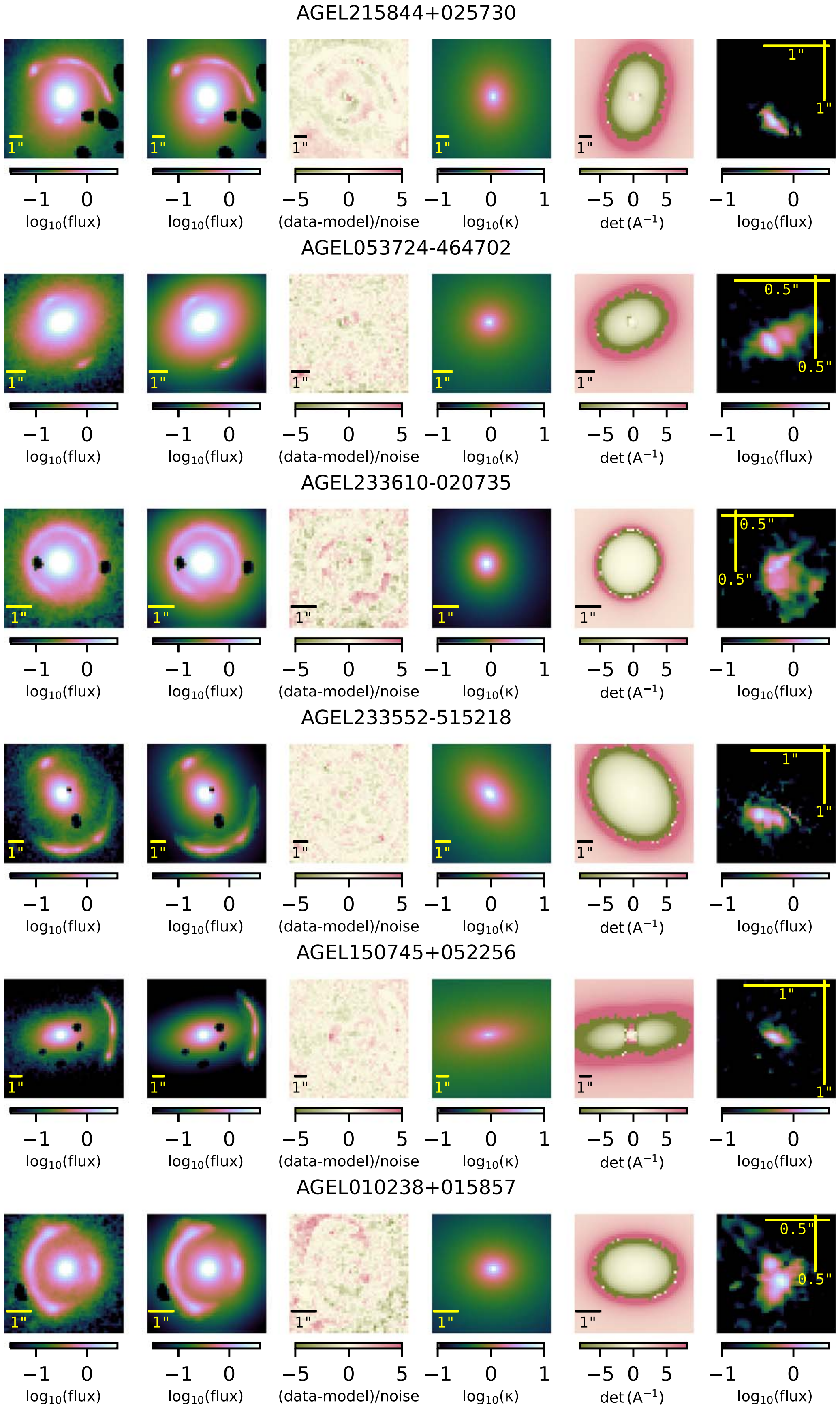

Figure A1. Lens modeling results for the remaining six `AGEL` lenses modeled here using GLEE. See Section 4.1 and Appendix A for details.

Table A1
Parameters for the Lens Mass Distribution, External Shear, and Lens Light Profile

Parameter	`AGEL` **2158**	`AGEL` **0537**	`AGEL` **2336**	`AGEL` **2335**	`AGEL` **1507**	`AGEL` **0142**	`AGEL` **0102**
	SPEMD						
$\gamma^{\rm lens}$	1.820 ± 0.014	1.810 ± 0.016	2.248 ± 0.042	2.020 ± 0.018	1.620 ± 0.018	2.208 ± 0.100	1.944 ± 0.028
$q_{\rm m}$	0.768 ± 0.004	0.904 ± 0.011	0.885 ± 0.010	0.703 ± 0.005	0.434 ± 0.006	0.617 ± 0.045	0.837 ± 0.010
$R_{\rm Eins}$ (arcsec)	3.271 ± 0.006	1.902 ± 0.003	1.392 ± 0.004	3.586 ± 0.009	2.875 ± 0.047	2.333 ± 0.044	1.494 ± 0.003
$\varphi_{\rm m}$ (rad, $+x$)	1.587 ± 0.009	0.268 ± 0.065	1.719 ± 0.045	2.249 ± 0.006	0.129 ± 0.002	3.029 ± 0.023	3.134 ± 0.024
	External shear						
$\gamma_{\rm ext}$	0.086 ± 0.003	0.069 ± 0.004	0.046 ± 0.003	0.037 ± 0.002	0.069 ± 0.005	0.028 ± 0.011	0.061 ± 0.005
$\varphi_{\rm ext}$ (rad, $+x$)	2.557 ± 0.012	2.059 ± 0.034	2.322 ± 0.027	2.208 ± 0.014	0.436 ± 0.034	1.690 ± 0.13	1.559 ± 0.018
	Sérsic profile 1						
$q_{\rm L,1}$	0.756 ± 0.002	0.766 ± 0.004	0.994 ± 0.005	0.698 ± 0.005	0.491 ± 0.003	0.711 ± 0.004	0.311 ± 0.006
$R_{\rm eff,1}$ (arcsec)	4.999 ± 0.032	0.336 ± 0.010	1.477 ± 0.014	4.010 ± 0.114	3.332 ± 0.037	2.741 ± 0.059	2.603 ± 0.001
$\varphi_{\rm L,1}$ (rad, $+x$)	1.323 ± 0.004	0.556 ± 0.009	2.045 ± 0.900	2.021 ± 0.007	0.173 ± 0.003	2.916 ± 0.007	1.423 ± 0.013
n_1	1.970 ± 0.057	1.604 ± 0.037	0.598 ± 0.021	3.422 ± 0.242	1.681 ± 0.03	3.232 ± 0.158	2.718 ± 0.001
A_1 (e^-/s)	0.226 ± 0.003	7.694 ± 0.257	0.417 ± 0.012	0.099 ± 0.005	0.206 ± 0.004	0.178 ± 0.007	0.677 ± 0.034
	Sérsic profile 2						
$q_{\rm L,2}$	0.846 ± 0.002	0.776 ± 0.002	0.956 ± 0.005	0.921 ± 0.013	0.967 ± 0.011	0.899 ± 0.014	0.960 ± 0.010
$R_{\rm eff,2}$ (arcsec)	0.451 ± 0.007	2.262 ± 0.021	0.267 ± 0.007	0.278 ± 0.010	0.287 ± 0.007	0.259 ± 0.007	0.234 ± 0.006
$\varphi_{\rm L,2}$ (rad, $+x$)	1.957 ± 0.012	0.553 ± 0.006	2.000 ± 0.061	2.459 ± 0.100	2.593 ± 0.232	0.059 ± 0.073	1.019 ± 0.128
n_2	1.681 ± 0.020	1.131 ± 0.045	1.760 ± 0.055	1.804 ± 0.063	1.613 ± 0.042	1.253 ± 0.059	1.196 ± 0.048
A_2 (e^-/s)	7.149 ± 0.107	0.467 ± 0.01	6.703 ± 0.256	3.823 ± 0.123	2.789 ± 0.082	3.705 ± 0.156	3.425 ± 0.129
	Single Sérsic fit						
$q_{\rm L}$	0.814 ± 0.001	0.766 ± 0.001	0.965 ± 0.002	0.766 ± 0.002	0.553 ± 0.001	0.744 ± 0.002	0.965 ± 0.004
$R_{\rm eff}$ (arcsec)	6.498 ± 0.048	2.409 ± 0.013	1.458 ± 0.015	3.042 ± 0.039	3.171 ± 0.025	2.213 ± 0.019	2.100 ± 0.042
$\varphi_{\rm L}$ (rad, $+x$)	1.478 ± 0.003	0.549 ± 0.003	2.020 ± 0.035	2.069 ± 0.005	0.164 ± 0.002	2.939 ± 0.004	0.607 ± 0.064
n	6.860 ± 0.023	4.952 ± 0.019	5.740 ± 0.044	6.196 ± 0.044	3.866 ± 0.026	5.091 ± 0.032	4.849 ± 0.058
A (e^-/s)	0.120 ± 0.002	0.397 ± 0.004	0.406 ± 0.008	0.145 ± 0.003	0.187 ± 0.003	0.252 ± 0.004	0.125 ± 0.004
	Circularized half-light radius of lens galaxy (in arcsec)						
$R_{\rm half,\ gal,\ eq}$	2.191 ± 0.079	0.881 ± 0.044	0.675 ± 0.042	1.736 ± 0.263	1.065 ± 0.045	1.259 ± 0.142	0.964 ± 0.082

Note. Here, $\gamma^{\rm lens}$ is the magnitude of the slope of the power-law density profile ($\rho \propto r^{-\gamma^{\rm lens}}$), $q_{\rm m}$ is the lens mass axis ratio, $R_{\rm Eins}$ is the projected Einstein radius along the major axis, $\varphi_{\rm m}$ is the position angle in radians measured anticlockwise from the positive x-axis, $\gamma_{\rm ext}$ is the external shear magnitude, $\varphi_{\rm ext}$ is the external shear angle in radians measured anticlockwise from the positive x-axis. These are followed by the parameters of the two Sérsic components (denoted by subscripts 1 and 2) of the total lens light profile, where $q_{\rm L}$ is the light axis ratio, $R_{\rm eff}$ is the effective half-light radius of the Sérsic profile along the major axis, $\varphi_{\rm L}$ is the lens light position angle, n is the Sérsic index, and A is the amplitude representing flux count rate at $R_{\rm eff}$. We also provide parameters for the single Sérsic fit to the total lens light. $R_{\rm half,gal,eq}$ is the overall circularized half-light radius of the lens galaxy. Mass and light centroids for `AGEL` 0537, `AGEL` 2335, `AGEL` 0142, and `AGEL` 0102 were linked during lens modeling. Mass and light centroids for `AGEL` 2158, `AGEL` 2336, and `AGEL` 1507 were not linked during modeling; however, both are found to be consistent within the observed image pixel resolution (±0.″08).

Appendix B
L&D versus Lensing-only Density Profile Slopes

Figure B1 compares the lensing-only density profile slopes with the slopes obtained using joint lensing and dynamical analysis. Figure B1 also shows a bisector fit, performed using the regression routine from Akritas & Bershady (1996), to quantify the correlation between the two measurements. The γ–z diagram with the L&D slopes for the `AGEL` pilot sample is shown in Figure B2. See Section 5.1 for more details.

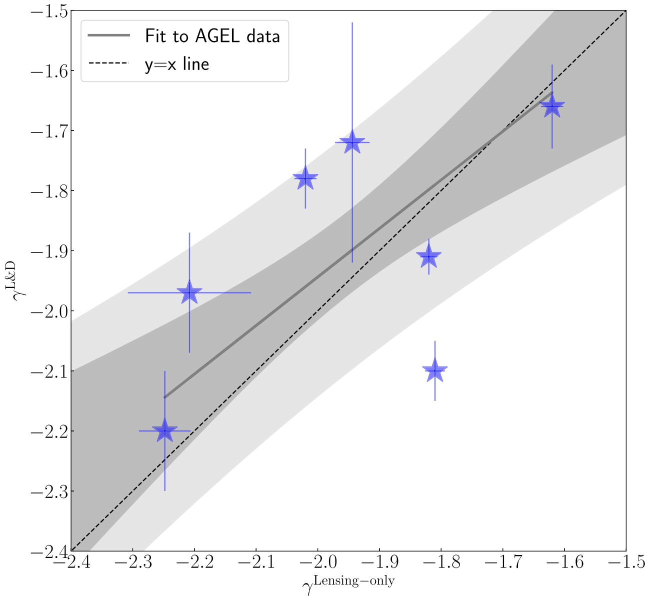

Figure B1. One-to-one comparison between total density profile slope of lenses in `AGEL` sample using the two methods: lensing-only and L&D. The gray line is a fit to the data: the dark gray shades show 1σ uncertainty in line slope and intercept, and the light shaded region shows 1σ scatter about the fit.

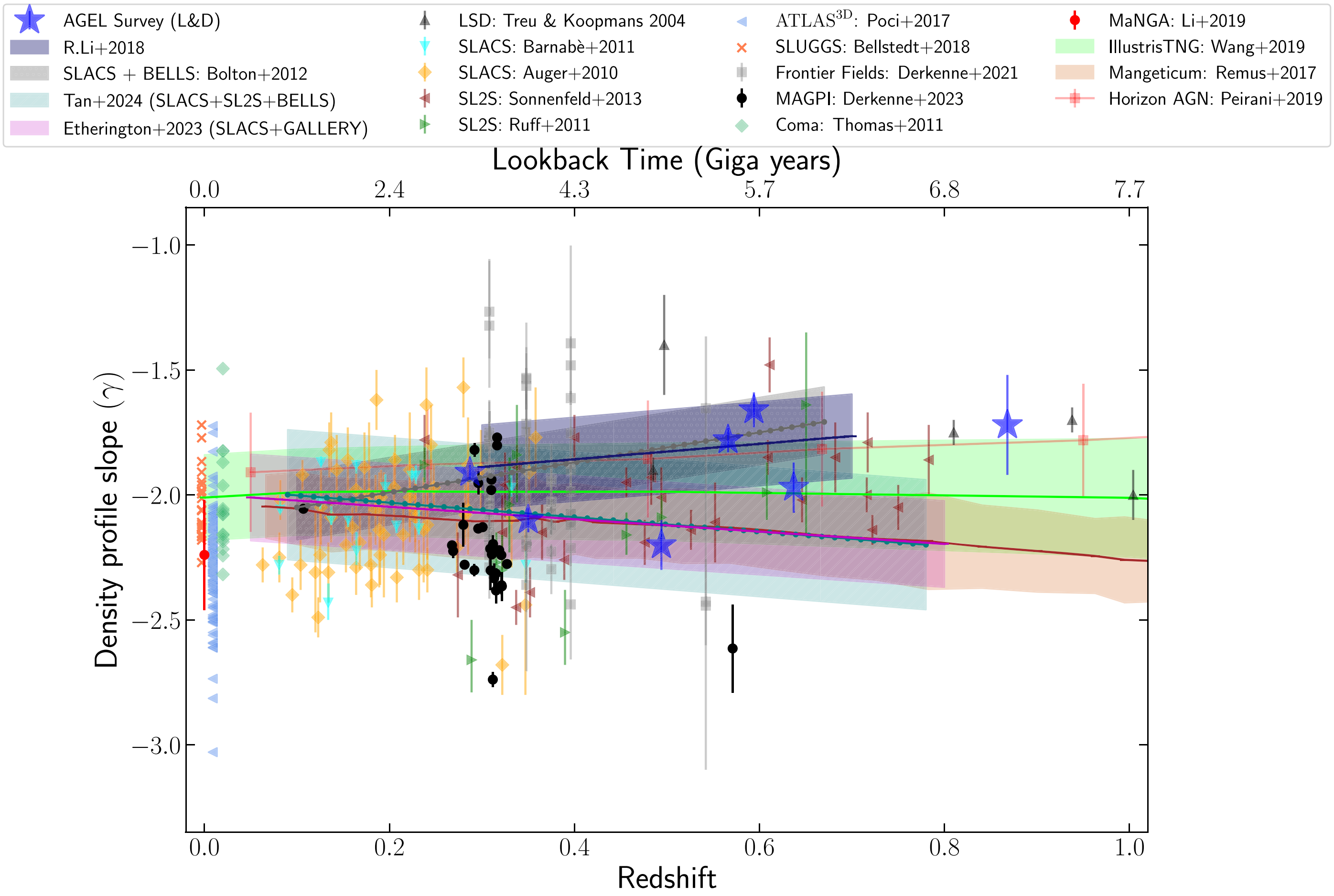

Figure B2. Same as Figure 4 but now representing L&D slopes for the `AGEL` pilot sample marked with blue stars.

ORCID iDs

Nandini Sahu https://orcid.org/0000-0003-0234-6585
Kim-Vy Tran https://orcid.org/0000-0001-9208-2143
Sherry H. Suyu https://orcid.org/0000-0001-5568-6052
Anowar J. Shajib https://orcid.org/0000-0002-5558-888X
Glenn G. Kacprzak https://orcid.org/0000-0003-1362-9302
Karl Glazebrook https://orcid.org/0000-0002-3254-9044
Tucker Jones https://orcid.org/0000-0001-5860-3419
Keerthi Vasan G. C. https://orcid.org/0000-0002-2645-679X
Tania M. Barone https://orcid.org/0000-0002-2784-564X
Geraint F. Lewis https://orcid.org/0000-0003-3081-9319
Sarah M. Sweet https://orcid.org/0000-0002-1576-2505
Sebastian Lopez https://orcid.org/0000-0003-0389-0902

References

Akritas, M. G., & Bershady, M. A. 1996, ApJ, 470, 706
Astropy Collaboration, Price-Whelan, A. M., Lim, P. L., et al. 2022, ApJ, 935, 167
Astropy Collaboration, Price-Whelan, A. M., Sipőcz, B. M., et al. 2018, AJ, 156, 123
Astropy Collaboration, Robitaille, T. P., Tollerud, E. J., et al. 2013, A&A, 558, A33
Auger, M. W., Treu, T., Bolton, A. S., et al. 2010, ApJ, 724, 511
Avila, R. J., Hack, W., Cara, M., et al. 2015, in ASP Conf. Ser. 495, Astronomical Data Analysis Software an Systems XXIV (ADASS XXIV), ed. A. R. Taylor & E. Rosolowsky (San Francisco, CA: ASP), 281
Barkana, R. 1998, ApJ, 502, 531
Barnabè, M., Czoske, O., Koopmans, L. V. E., Treu, T., & Bolton, A. S. 2011, MNRAS, 415, 2215
Barnes, J. E., & Hernquist, L. E. 1991, ApJL, 370, L65
Bellstedt, S., Forbes, D. A., Romanowsky, A. J., et al. 2018, MNRAS, 476, 4543
Binney, J. 1978, MNRAS, 183, 501
Binney, J., & Mamon, G. A. 1982, MNRAS, 200, 361
Birrer, S. 2021, ApJ, 919, 38
Birrer, S., & Amara, A. 2018, PDU, 22, 189
Birrer, S., Shajib, A. J., Galan, A., et al. 2020, A&A, 643, A165
Birrer, S., Shajib, A. J., Gilman, D., et al. 2021, JOSS, 6, 3283
Blandford, R. D., & Kochanek, C. S. 1987, ApJ, 321, 658
Blandford, R. D., & Narayan, R. 1992, ARA&A, 30, 311
Blumenthal, G. R., Faber, S. M., Primack, J. R., & Rees, M. J. 1984, Natur, 311, 517
Bolton, A. S., Brownstein, J. R., Kochanek, C. S., et al. 2012, ApJ, 757, 82
Bolton, A. S., Burles, S., Koopmans, L. V. E., Treu, T., & Moustakas, L. A. 2006, ApJ, 638, 703
Brodie, J. P., Romanowsky, A. J., Strader, J., et al. 2014, ApJ, 796, 52
Brownstein, J. R., Bolton, A. S., Schlegel, D. J., et al. 2012, ApJ, 744, 41
Bundy, K., Bershady, M. A., Law, D. R., et al. 2015, ApJ, 798, 7
Cabanac, R. A., Alard, C., Dantel-Fort, M., et al. 2007, A&A, 461, 813
Cappellari, M., 2012 pPXF: Penalized Pixel-Fitting stellar kinematics extraction, Astrophysics Source Code Library, ascl:1210.002
Cappellari, M. 2016, ARA&A, 54, 597
Cappellari, M. 2023, MNRAS, 526, 3273
Cappellari, M., Emsellem, E., Bacon, R., et al. 2007, MNRAS, 379, 418
Chen, C.-Y., Hwang, C.-Y., & Ko, C.-M. 2016, ApJ, 830, 123
Ciambur, B. C. 2016, PASA, 33, e062
Ciotti, L., & Bertin, G. 1999, A&A, 352, 447
Coccato, L., Gerhard, O., Arnaboldi, M., et al. 2009, MNRAS, 394, 1249
Derkenne, C., McDermid, R. M., Poci, A., et al. 2021, MNRAS, 506, 3691
Derkenne, C., McDermid, R. M., Poci, A., et al. 2023, MNRAS, 522, 3602
Dunkley, J., Bucher, M., Ferreira, P. G., Moodley, K., & Skordis, C. 2005, MNRAS, 356, 925
Dutton, A. A., Brewer, B. J., Marshall, P. J., et al. 2011, MNRAS, 417, 1621
Dutton, A. A., & Treu, T. 2014, MNRAS, 438, 3594
Eisenstein, D. J., Weinberg, D. H., Agol, E., et al. 2011, AJ, 142, 72
Ertl, S., Schuldt, S., Suyu, S. H., et al. 2023, A&A, 672, A2
Etherington, A., Nightingale, J. W., Massey, R., et al. 2023, MNRAS, 521, 6005
Falco, E. E., Gorenstein, M. V., & Shapiro, I. I. 1985, ApJL, 289, L1
Filipp, A., Shu, Y., Pakmor, R., Suyu, S. H., & Huang, X. 2023, A&A, 677, A113
Foreman-Mackey, D., Hogg, D. W., Lang, D., & Goodman, J. 2013, PASP, 125, 306
Forrest, B., Wilson, G., Muzzin, A., et al. 2022, ApJ, 938, 109
Foster, C., Mendel, J. T., Lagos, C. D. P., et al. 2021, PASA, 38, e031
Guo, Q., & White, S. D. M. 2008, MNRAS, 384, 2
Halkola, A., Hildebrandt, H., Schrabback, T., et al. 2008, A&A, 481, 65
Halkola, A., Seitz, S., & Pannella, M. 2006, MNRAS, 372, 1425
Harris, C. R., Millman, K. J., van der Walt, S. J., et al. 2020, Natur, 585, 357
Humphrey, P. J., & Buote, D. A. 2010, MNRAS, 403, 2143
Hunter, J. D. 2007, CSE, 9, 90
Kirkpatrick, S., Gelatt, C. D., & Vecchi, M. P. 1983, Sci, 220, 671
Kochanek, C. S. 2020, MNRAS, 493, 1725
Koopmans, L. V. E., Bolton, A., Treu, T., et al. 2009, ApJL, 703, L51
Koopmans, L. V. E., & Treu, T. 2004, in The Lenses Structure & Dynamics Survey, Astrophysics and Space Science Library, Vol. 301, ed. M. Plionis (Berlin: Springer), 23
Koopmans, L. V. E., Treu, T., Bolton, A. S., Burles, S., & Moustakas, L. A. 2006, ApJ, 649, 599
Krist, J. E., Hook, R. N., & Stoehr, F. 2011, Proc. SPIE, 8127, 81270J
Kronawitter, A., Saglia, R. P., Gerhard, O., & Bender, R. 2000, A&AS, 144, 53
Li, R., Li, H., Shao, S., et al. 2019, MNRAS, 490, 2124
Li, R., Shu, Y., & Wang, J. 2018a, MNRAS, 480, 431
Li, R., Wang, J., Shu, Y., & Xu, Z. 2018b, ApJ, 855, 64
McKerns, M. M., Strand, L., Sullivan, T., Fang, A., & Aivazis, M. A. G. 2012, arXiv:1202.1056
Merritt, D. 1985, AJ, 90, 1027
Mihos, J. C., & Hernquist, L. 1994, ApJL, 425, L13
Mukherjee, S., Koopmans, L. V. E., Metcalf, R. B., et al. 2021, MNRAS, 504, 3455
Naab, T., Johansson, P. H., Ostriker, J. P., & Efstathiou, G. 2007, ApJ, 658, 710
Newman, A. B., Ellis, R. S., & Treu, T. 2015, ApJ, 814, 26
Oser, L., Ostriker, J. P., Naab, T., Johansson, P. H., & Burkert, A. 2010, ApJ, 725, 2312
Osipkov, L. P. 1979, PAZh, 5, 77
Peirani, S., Sonnenfeld, A., Gavazzi, R., et al. 2019, MNRAS, 483, 4615
Poci, A., Cappellari, M., & McDermid, R. M. 2017, MNRAS, 467, 1397
Remus, R.-S., Dolag, K., Naab, T., et al. 2017, MNRAS, 464, 3742
Ruff, A. J., Gavazzi, R., Marshall, P. J., et al. 2011, ApJ, 727, 96
Saglia, R. P., Kronawitter, A., Gerhard, O., & Bender, R. 2000, AJ, 119, 153
Sánchez-Blázquez, P., Peletier, R. F., Jiménez-Vicente, J., et al. 2006, MNRAS, 371, 703
Schneider, P., Ehlers, J., & Falco, E. E. 1992, Gravitational Lenses (Berlin: Springer)
Schneider, P., & Sluse, D. 2013, A&A, 559, A37
Sérsic, J. L. 1963, BAAA, 6, 41
Shajib, A. J., Glazebrook, K., Barone, T., et al. 2022a, ApJ, 938, 141
Shajib, A. J., Mozumdar, P., Chen, G. C. F., et al. 2023, A&A, 673, A9
Shajib, A. J., Treu, T., Birrer, S., & Sonnenfeld, A. 2021, MNRAS, 503, 2380
Shajib, A. J., Vernardos, G., Collett, T. E., et al. 2022b, arXiv:2210.10790
Sheinis, A. I., Bolte, M., Epps, H. W., et al. 2002, PASP, 114, 851
Shu, Y., Bolton, A. S., Mao, S., et al. 2016, ApJ, 833, 264
Somerville, R. S., & Davé, R. 2015, ARA&A, 53, 51
Sonnenfeld, A., Gavazzi, R., Suyu, S. H., Treu, T., & Marshall, P. J. 2013a, ApJ, 777, 97
Sonnenfeld, A., Nipoti, C., & Treu, T. 2014, ApJ, 786, 89
Sonnenfeld, A., Treu, T., Gavazzi, R., et al. 2013b, ApJ, 777, 98
Suyu, S. H., Auger, M. W., Hilbert, S., et al. 2013, ApJ, 766, 70
Suyu, S. H., & Halkola, A. 2010, A&A, 524, A94
Suyu, S. H., Hensel, S. W., McKean, J. P., et al. 2012, ApJ, 750, 10
Suyu, S. H., Marshall, P. J., Hobson, M. P., & Blandford, R. D. 2006, MNRAS, 371, 983
Tan, C. Y., Shajib, A. J., Birrer, S., et al. 2024, MNRAS, 530, 1474
Thomas, D., Steele, O., Maraston, C., et al. 2013, MNRAS, 431, 1383
Thomas, J., Saglia, R. P., Bender, R., et al. 2011, MNRAS, 415, 545
Tran, K.-V. H., Harshan, A., Glazebrook, K., et al. 2022, AJ, 164, 148
Treu, T. 2010, ARA&A, 48, 87
Treu, T., & Koopmans, L. V. E. 2002, ApJ, 575, 87
Treu, T., & Koopmans, L. V. E. 2004, ApJ, 611, 739
van de Sande, J., Bland-Hawthorn, J., Fogarty, L. M. R., et al. 2017, ApJ, 835, 104
Vernet, J., Dekker, H., D'Odorico, S., et al. 2011, A&A, 536, A105
Virtanen, P., Gommers, R., Oliphant, T. E., et al. 2020, NatMe, 17, 261
Wang, Y., Vogelsberger, M., Xu, D., et al. 2019, MNRAS, 490, 5722
Wang, Y., Vogelsberger, M., Xu, D., et al. 2020, MNRAS, 491, 5188
Weijmans, A.-M., Krajnović, D., van de Ven, G., et al. 2008, MNRAS, 383, 1343
White, S. D. M., & Frenk, C. S. 1991, ApJ, 379, 52
Xu, D., Springel, V., Sluse, D., et al. 2017, MNRAS, 469, 1824